Breakdown of diffusion approximation for light propagation in nano-porous GaP sponges

Master's thesis
Master of Science, Nanotechnology
Sanli Ebrahimi Pour Faez
June 2007

Breakdown of diffusion approximation for light propagation in nano-porous GaP sponges

Master's thesis[1]
Master of Science, Nanotechnology
Sanli Ebrahimi Pour Faez
June 2007

Graduation committee:
Dr. P.M. Johnson (AMOLF)
Prof. dr. A. Lagendijk (AMOLF and COPS)
Dr. D.A. Mazurenko (RuG)
Dr. A.P. Mosk (COPS)
Dr. W.G. van der Wiel (MESA$^+$)

This work was done at AMOLF:
FOM Institute for Atomic and Molecular Physics (AMOLF)
Center for Nanophotonics
P.O. Box 41883
1009 DB Amsterdam

and also at COPS:
Complex Photonic Systems
MESA$^+$ Institute for Nanotechnology
Faculty of Science and Technology
University of Twente
P.O. Box 217
7500 AE Enschede

[1]The electronic document is available at www.sanlifaez.com.

Acknowledgements

I like to thank Ad Lagendijk for his perceptive supervision and insightful way of teaching. The optical nonlinearity experiments were started by Dmitry Mazurenko. He introduced the subject to me and it was with his help that I got the setup working. For this setup, we used essential equipment from the group of Photonic Bandgaps at Amolf. I thank Willem Vos for his collaboration and Philip Harding, Tijmen Euser, Alex Hartsuiker, and Bart Husken for sharing their lab-space and experiment-time. Patrick Johnson has been always a patient listener and a clever suggester. He took the role of my daily supervisor after Dmitry went to Groningen. I thank Patrick again for carefully correcting the first draft of my thesis. Hereby I also thank all my graduation committee members for deliberately reading the whole thesis.

I have experienced the most healthy scientific teamwork spirit during my presence in COPS and Photon Scattering, and in vicinity of Photonic Bandgaps. I would like to thank all the people mentioned above, together with Allard, Leon, Cock, Tom, Bernard, Willem T., Karen, Ivo, Wouter, Paolo, Oscar, Ivan, Vitaly, Merel, Steven, Pedro, Otto, and Charles. Frequently, Paolo and Otto assisted me in the lab. Discussions with Tom, Bernard and Pedro helped me catch up in the theory. Tom made writing much easier for me with sharing his well-organized thesis template. The nanophotonics colloqium and group discussions at Amolf have been the best place to look over the hedge. I also like to thank my intimate colleagues and friends, Ramy, Elbert, and Frerik in COPS, and Tian, Dhirendra, Abishek, Winbin, and Jaap. I like to thank Theo Nieuwenhuizen for his kindness.

Many people were involved in easing my education. In University of Twente, Rik Akse, Karen Munnink, Martin Bennink and Wilfred van der Wiel helped me in my master program. Wilfred has been always a very keen mentor for me. In Leiden University, Eric Eliel and the group of QOQI showed the best hospitality during my internship. The personnel support and technical staff at Amolf have always been very helpful and quick. My studies were supported by the Shell Centenary Scholarship Fund.

I like to send my regards to my family for their all-time support and heartening. And my dearest Bahar, you have manifested the highest level I could imagine for *being together*. Thank you for your love, your enthusiasm in my progress, being patient with my untidy schedule, reading my thesis, fruitful scientific discussions, and more; I can hardly name everything I have to thank you for.

Sanli

Abstract

Highly-scattering materials have been the subject of research for more than a hundred years, but the enthusiasm in the subject has never declined. Most of the observed phenomena have been described within the photon diffusion approximation. The diffusion approximation will break down in the extreme case where interference effects become so significant that a phase transition to Anderson localization regime happens. Nano-porous GaP sponges are of particular interest for the observation of this transition.

In this thesis both stationary and non-stationary measurements on Nano-porous GaP are presented. A new experimental method is proposed and introduced as the *effusion microscopy*. This method is shown to give valuable information about the effect of anisotropic diffusion as well as non-diffusive behaviors. Effusion microscopy has revealed that a few of our samples deviate from the diffusive regime, and possibly show signs of Anderson localization.

Second-harmonic generation in nano-porous GaP slabs has also been studied experimentally. Total second-harmonic yield measurements and the ratio of second-harmonic light emitted from the front and back side of the sample were compared with the theoretical predictions of the non-stationary diffusion approximation. It has been shown that most of the samples show behavior consistent with the photon diffusion model. However, a subset of the samples deviate up to a factor of 10 times from diffusive behavior. These cases are highlighted and the connection to the Anderson localization of light is expressed.

Contents

1 Introduction: Light in opaque material **15**
1.1 Light is a wave . . . 15
1.2 From scattering to diffusion . . . 16
1.3 Anderson localization . . . 16
1.4 In this thesis . . . 17

2 Diffusion theory of light **19**
2.1 Diffusion approximation . . . 19
2.1.1 Light is made of particles . . . 20
2.1.2 Observable quantities . . . 21
2.1.3 Validity of photon diffusion theory . . . 22
2.2 Stationary regime . . . 23
2.2.1 Poisson equation . . . 23
2.2.2 Boundary conditions . . . 23
2.2.3 Method of images . . . 24
2.2.4 Anisotropic diffusion . . . 24
2.3 Slab geometry . . . 25
2.3.1 Transmittance for plane wave . . . 25
2.3.2 Effusion from slab for point source . . . 26
2.4 Half-slab geometry . . . 27
2.4.1 Transverse effusion for a point source . . . 28
2.5 Non-stationary regime . . . 29
2.5.1 General solution in slab geometry . . . 29
2.6 Optical nonlinearity in opaque material . . . 30
2.6.1 Nonlinear mechanism for diffusive photons . . . 30
2.6.2 Stationary solution . . . 31
2.6.3 Non-stationary solution . . . 31

3 Nano-porous GaP **35**
3.1 History of GaP sponges . . . 35
3.2 Fabrication procedure . . . 36
3.3 Sample characterization . . . 37
3.3.1 Quantifying pore size . . . 37
3.3.2 Summary of properties for investigated samples . . . 38

4 Stationary effusion pattern **41**
4.1 Introduction . . . 41
4.2 Diffusion of a focused beam in slab . . . 42
4.2.1 Transmittance microscopy setup . . . 42
4.2.2 Extracting the mean free path . . . 43
4.2.3 Extracting the anisotropy . . . 44
4.2.4 Spatial spikes in effusion function . . . 45
4.3 Transverse effusion from half-slabs . . . 45
4.3.1 Transverse effusion microscopy setup . . . 47
4.3.2 Deviation from the diffusive regime . . . 47

5 Nonlinear optics with porous GaP **53**
5.1 Introduction . . . 53
5.2 Yield measurements . . . 54
5.2.1 Integrating sphere setup . . . 55
5.2.2 Dependence on incident power . . . 55
5.3 Far-field distribution . . . 56
5.3.1 Backward-forward ratio . . . 56
5.3.2 Deviation from diffusion theory prediction . . . 57
5.4 Internal distribution . . . 59
5.4.1 Transverse effusion at second-harmonic frequency . . . 59
5.4.2 Special behavior in outliers . . . 60

6 Conclusion **61**
6.1 Summary of experiments . . . 61
6.2 To diffuse or not to diffuse . . . 62
6.2.1 Confirmation cases . . . 62
6.2.2 Violation cases . . . 63
6.3 Follow up research . . . 63

Bibliography **64**

A Compact setup for recording enhanced backscattering **69**

B Setup for total transmission measurement **73**

Index **75**

List of Abbreviations and Symbols

EBS	Enhanced backscattering
SEM	Scanning electron micrograph/Scanning electron microscopy
$C_{\hat{\mathbf{x}}}$	Autocorrelation function along $\hat{\mathbf{x}}$
D	Diffusion constant
$\bar{D}$	Diffusion tensor
E	Static electric field
E_f	Enhancement factor (of EBS)
I	Effusion function
I_0	Incident intensity
$I^{\perp}$	Transverse effusion function
L	Sample thickness
L_a	Absorption length
L_c	Coherency length
L_l	Localization length
P_0	Incident power
$R^{(2)}$	Second-harmonic radiation in backward direction
S	Distribution of diffusive-photon source
$S^{(2)}$	Distribution of second-harmonic diffusive-photon source
T	Transmittance
$T^{(2)}$	Second-harmonic radiation in forward direction
$T^{\perp}$	Total transverse effusion
d	Pulse length
k_0	Free-space wave number
ℓ	Mean free path
n	Refractive index
t_s	Thouless time, time of transition to stationary diffusion regime
u	Diffusive energy density at fundamental frequency
$u^{(2)}$	Diffusive energy density at second-harmonic frequency
z_s	Distance from source to the edge of sample
Γ	Effective nonlinear coefficient
Π	Normalized pulse-envelope function
η	Backward-forward ratio of total second-harmonic radiation
λ_0	Wavelength of light in vacuum

ϕ Electrostatic potential

List of Figures

2.1 Schematic of diffusion approximation for light 20
2.2 Method of images used for solving diffusion equation 27
2.3 Effect of higher order image charges 29
2.4 Stationary solution for second-harmonic energy distribution 31
2.5 Non-stationary solution for second-harmonic energy distribution 33

3.1 SEM of nanoporous GaP surface 36
3.2 Mean free path spectrum 37
3.3 Measuring pore size from SEM 38

4.1 Schematic setup for transmittance and transverse effusion microscopy . . . 42
4.2 Example of effusion function measurement 43
4.3 Measured effusion function compared with diffusion theory 44
4.4 Spikes in transmittance pattern 46
4.5 Example of transverse effusion pattern measurement 47
4.6 Deviation of total transverse effusion from diffusive behavior 48
4.7 Deviation of peak effusion value from diffusive behavior 49
4.8 Comparison between diffusive and non-diffusive effusion patterns 50
4.9 Prediction of source position base on transverse effusion function 51

5.1 Schematic setup for measuring second-harmonic generation 54
5.2 Quadratic dependence of second-harmonic generation 56
5.3 Backward-forward ratio of second-harmonic radiation 57
5.4 Second-harmonic generation yield for several samples 58
5.5 Example of second-harmonic transverse effusion function 59

A.1 Schematic setup for measuring enhanced backscattering 70
A.2 Comparison of EBS measurements of two setups 71

B.1 Schematic setup for measuring total transmission 74

CHAPTER 1

Introduction: Light in opaque material

1.1 Light is a wave

Electromagnetic waves were first predicted by James Clerk Maxwell and subsequently demonstrated by Heinrich Hertz. Maxwell derived a wave form of the electric and magnetic equations, revealing the wave-like nature of electric and magnetic fields, and their symmetry. Maxwell concluded that light itself is an electromagnetic wave, because the speed of electromagnetic waves predicted by the wave equation coincided with the measured speed of light.

Electromagnetic waves, like the other solutions to Maxwell's equations, must fulfill a specific set of boundary conditions and obey principles of superposition. These properties cause various phenomena including interference and refraction. In refraction, a wave crossing from one medium to another of different density alters its speed and direction upon entering the new medium. The ratio of the refractive indices of the media determines the degree of refraction, summarized by Snell's law. Due to the frequency dependence of the refractive indices of most materials, white light disperses into a visible spectrum when it refracts, for example through a prism. Interference is the superposition of two or more waves resulting in a new wave pattern. If the fields have vector components in the same direction, they constructively interfere, while components in opposite directions lead to destructive interference.

In vacuum or in homogeneous medium, light propagates in the form of a superposition of spherical waves, which is well known as Huygens' principle. Light interacts with objects such as atoms, dielectrics or metals mostly by three major processes: radiation, absorption, and scattering. Radiation is caused by accelerating charged particles or electric currents. In absorption, due to presence of the object, the energy in the electromagnetic field of light is transformed into other forms of kinetic or potential energy, such as chemical energy, heat, and electromotive force. In the process of light scattering, the object radiates light, coherently, in response to being exposed by light from another source. Scattering of light can be either elastic or inelastic. In elastic scattering the light energy is conserved. The incident

light and the radiated light can generally interfere. In principle, these three processes can be designed for any kind of wave.

1.2 From scattering to diffusion

Transport of light through non-absorbing opaque objects such as fog, clouds, milky liquids, white paint, paper, and porcelain, can be describes as a collective effect of many scattering events. The amount of light that can pass through such an opaque object depends on the density of scattering events and the scattering strength of each event. In this model light is propagating freely (as in vacuum or a transparent object) between two successive scattering events, but still can interfere with itself. If one neglects interference effects, this process is similar to particle transport in a gas such as the spread of odor in air. The average distance between two scattering events is referred to as mean free path. If the mean free path is much larger than the wavelength of light, interference effects have in average little influence on the outcome of many types of measurements and the transport of light can be described by diffusion.

The study of diffuse wave transport was first undertaken by astrophysicists. They wanted to understand how radiation created in the center of stars is affected when it traverses an interstellar cloud. Well-known books in this field were written by Chandrasekhar (1960) and Van de Hulst (1980). Many properties of diffuse light are well known. Nowadays the diffusive transport of visible light through human tissue is being used as a noninvasive technique to detect tumors[1].

With a more rigorous treatment of light diffusion, even some interference effects can be very well described. One of these phenomena is enhanced backscattering. Enhanced backscattering is a result of the most robust interference effects that survives multiple scattering. When a strongly scattering object is illuminated with coherent light (such as a laser) the constructive interference of time-reversed paths, on average, leads to a net increase of light transport in exactly the backward direction. The amount of enhancement is twice the background scattered intensity when the incident light is incoherent (like a candle).

Enhanced backscattering can be observed for any type of wave that experiences multiple scattering. Acoustic waves that scatter from solid objects or shallow surface waves on a liquid that scatter from height variation of their bath can also exhibit enhancement in the backward direction. For quantum mechanical wave-function this phenomena is reffered to as as weak localization[2]. Enhanced backscattering of light from a solid object was observed in 1985 by van Albada and Lagendijk[3] and at the same time by Wolf and Maret[4].

1.3 Anderson localization

Anderson localization, also known as strong localization, refers to the absence of diffusion of waves in a random medium due to interference effects. This phenomenon was named after Philip Warren Anderson, who suggested the possibility of electron localization inside a semiconductor, provided that the degree of randomness of the impurities or defects is sufficiently large[5]. Anderson localization is a general wave phenomenon that applies to the transport of electromagnetic waves, acoustic waves[6], quantum waves and spin waves[7]. Very recently, it has been exhibited also in Bose-Einstein condensates[8, 9].

While weak localization is considered to be the precursor effect to Anderson localization, they correspond to two different phases of light propagation. Weak localization can be observed at any scattering strength as a result of wave interference between multiple-scattering paths inside the material. Anderson localization can be observed only in extremely strongly-scattering media in which the severity of interference effects prevents the energy of the waves from penetrating the random medium.

In the Anderson localization regime only localized modes exist, while in the diffusive regime extended modes convey the wave. In a localized region the stationary intensity distribution typically decays exponentially over one localization length, whereas in a diffusive region the stationary intensity distribution drops as a power law.

In one- and two-dimensional scattering potentials the states are always localized. The localization length decreases at lower values of randomness. In three dimensions a phase transition from the extended to the localized state can occur at the limit of the mean free path becoming smaller than the wavelength. Yet for a finite sample the localization length can be much larger than the system size, in which case the states appear to be extended and the conductance does not vanish. In that case, special precursors should be investigated to reveal the onset of Anderson localization. Following these precursors, deviation from classical diffusion was measured by transmittance measurement in highly scattering dielectric slabs with varying thicknesses[10].

De Raedt, Lagendijk, and de Vries predicted a special case of Anderson localization, which is called transverse localization, in objects that are randomly scattering only in two directions, but coherently transport light in the third orthogonal direction[11]. Fiber bundles are an example for such an object. This phenomenon was recently observed in disordered two-dimensional photonic lattices[12]. So far, this is the first observation of light localization in real time, rather than its indirect deduction from time-resolved transmission spectroscopy.

Direct observation of three-dimensional Anderson localization in real time has been the subject of much effort in the last 20 years, but has not yet reported. Nano-porous gallium phosphate sponges are among the most promising materials for this observation. The experiments described in this thesis may finally lead to the achievement of this quest.

1.4 In this thesis

To investigate a deviation from the diffusive regime in highly scattering objects, the diffusive properties need to be carefully understood. For that reason, a brief overview of photon diffusion formalism is introduced in chapter 2. Both stationary and non-stationary solutions are introduced. The effect of anisotropic scattering is briefly mentioned. A simplified nonlinear mechanism is used to model diffusive distribution of optical second-harmonic generation inside an opaque object.

Fabrication and characterization of nano-porous GaP sponges is described in chapter 3. The scattering properties of the samples used for experiments in this thesis are also listed. Newly developed stationary linear experiments on nano-porous GaP slabs are reported in chapter 4 and nonlinear-optical studies on these samples is presented in chapter 5. While most of the samples show behavior consistent with the photon diffusion model, a subset of samples deviate from diffusive behavior in both stationary and non-stationary experiments. These cases are highlighted and the connection to the Anderson localization of light is expressed.

CHAPTER 2

Diffusion theory of light

In this chapter I discuss diffusion-theory solutions to various linear and nonlinear processes in opaque material. First I present the diffusion equation for light scattering in opaque material and discuss its limits of validity. I consider both stationary and non-stationary regimes in various configurations of the sample and light source. I use the method of images for solving stationary cases in a slab and a half-slab for focused incident beam. Then I introduce the optical nonlinear mechanism in opaque materials and present a solution for the nonlinear response of opaque slab to short pulses.

2.1 Diffusion approximation

Diffusion is the net migration of particles, heat or energy from an area where the concentration is high to an area that has low concentration as a result of random interactions. Heat conduction and electric conduction in metals, spread of odor in air, or marking a paper with ink are examples of diffusion. It is possible to apply the concept of diffusion to a continuous field if the evolution of the field distribution or a function of that, which is another field by itself, obeys the diffusion equation. The diffusion equation in homogenous and isotropic media is most generally written as

$$\frac{\partial}{\partial t}\Psi(\mathbf{r},t) - D\nabla^2\Psi(\mathbf{r},t) = C(\mathbf{r},t). \tag{2.1}$$

Here $\Psi(\mathbf{r},t)$ is the scalar-field function and $C(\mathbf{r},t)$ denotes the distribution of sources, and sinks for the diffusive quantity. D is the diffusion constant that depends on the interaction between the field and the medium.

This definition of diffusion imposes, immediately, certain restrictions for the measurable quantities. First, the diffusion equation is continuous and it should be applied to continuous fields. In other words it is blind to fluctuations at the discrete level. Second, the assumption of homogeneity pin-points a length-scale below which this equation is not applicable. That

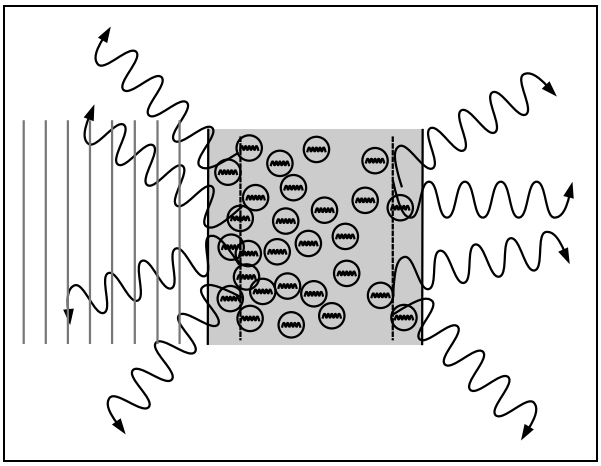

Figure 2.1: *In diffusion approximation for light scattering, all the information is carried by particle-like objects, photons, that scatter randomly and do not interfere. For modeling external sources incident on opaque object an isotropic source of diffusive photons is assumed to exist one mean free path from the surface of the object. Diffusive photons radiate as propagating waves at the surface.*

is roughly the length-scale at which the microscopic details of the medium show up. In experiments one should note that the diffusion equation is statistically correct and single realizations should always be ensemble-averaged in order to give a measure of diffusive quantities. In the following paragraphs we discuss how the diffusion approximation may be applied to electromagnetic waves.

In dense fog, a square array of lamps cannot be distinguished from a single lamp with an equal total brightness, although both can be seen as present. In this situation even a very good telescope cannot help. The elements of the array become distinguishable if the fog becomes less dense or if we go close enough to the source. In absence of absorption, multiple scattering is responsible for obscuring the shape of the light source. The number of scattering events that a detected piece of light has experienced, increases with the density of scatterers and the distance of the source from the detector. In such a medium, under certain criteria which will be addressed in section 2.1.3, much of the information from the source reaches the detector as if it were transported by discrete carriers performing a random-walk. Despite the randomization process, the signal of the detector may give information about the source luminescence, irradiance noise[13], or even the phase retardation of a phase-engineered source[14]. The average evolution of the density of these information carriers follows the diffusion equation.

2.1.1 Light is made of particles

In a non-absorbing opaque medium, when a plane wave of light propagates into the medium, the average propagation distance after which it loses all the information about its original direction is denoted by one extinction mean free path, ℓ_s. The average distance between two scattering events happening to a ray of light is called the Boltzmann mean free path, ℓ_{B}. For isotropic scatterers, these two quantities are equal. As, in this thesis, we are only considering isotropic scatterers, I define a common quantity as mean free path, $\ell = \ell_s = \ell_{\mathrm{B}}$.

For dealing with external sources, which are incident on opaque regions, an effective isotropic source of diffusive carriers is assumed to exist within one mean free path from the

boundaries of that region, i.e. the external beam penetrates one mean free path into the sample, see figure 2.1. In general the diffusion equation cannot be applied to this skin layer. Once the light has entered the bulk, the diffusive quantities obey the diffusion equation. Wherever the light exits the opaque region is assumed a boundary. Setting the boundary conditions is essential to solve the diffusion equation.

When using a continuous wave laser as the light source, the spatial coherency of this particle-like carriers is much larger than typical system sizes. It means the phase relation between the carriers holds even after many scattering events[1]. As a result, the diffusive intensity can interfere and build up an extended three dimensional speckle pattern. Inside and on the surface of the medium each bright spot (one speckle) has a spatial extension in the order of the wavelength and can be filtered out by averaging over a volume or an area larger than the speckle size. Far from the sample one speckle is better defined as a fraction of spherical angle around the sample. They can be visualized by projecting on a screen far from the sample. The speckle size is then the smallest angle between two neighboring speckles at which their projected images on the screen are still distinguishable. Far enough from the sample, the projection of a speckle may become larger than effective area of a detector.

Analysis of experimental results often requires to average the fluctuations in the light intensity due to the speckles. Experimentally, there are two major methods for averaging out the speckle pattern. First is to use a wide-bandwidth source, which minimizes the coherency length to a scales smaller than the sample size. The second solution is ensemble averaging over many realizations of scatterer's positions. This practically means shaking, relative to the beam, the whole sample when it is rigid, or its elements when it is in form of a suspension.

As quantized bits of light have already a given name, photon, from now on we use the same expression for the particle-like diffusive carriers, which obey the diffusion equation. The diffusion approximation for propagation of light in an opaque medium is then shortly called, the photon diffusion theory. It should be emphasized that this common nomenclature does not mean that the quantum optical properties of light are incorporated in the diffusion approximation.

2.1.2 Observable quantities

Formalizing the suitable diffusion equation in an opaque medium depends on the measurable quantity of interest. This quantity can be the energy density, the transmittance fluctuation or the phase information. As in the following chapters we are always dealing with the intensities, I write the diffusion equation for the average optical energy density inside a non-dissipative opaque material, $u(\mathbf{r}, t)$, which in the case of narrow bandwidth[2] is directly proportional to the diffusive-photon concentration. This equation then reads

$$\frac{\partial}{\partial t}u(\mathbf{r}, t) - D\nabla^2 u(\mathbf{r}, t) = S(\mathbf{r}, t), \tag{2.2}$$

where $S(\mathbf{r}, t)$ is the distribution function for sources of diffusive photons. For isotropic medium, $D = v_E\ell/3$, where v_E is the average energy velocity in the medium. Given the

[1] I don't discuss here inelastic scattering which may scramble the phase relation even after a single scattering.

[2] by narrow bandwidth I mean a frequency range in which dispersion and variation of scattering strength is negligible.

proper boundary conditions and the source distribution, we can solve the diffusion equation for average energy density distribution. Here I introduce the *effusion function* $I(\mathbf{r}, t)$ that is equal to the light radiation per unit of surface area at any point on the surface. The effusion function is defined as

$$I(\mathbf{r}, t) = [D\nabla u(\mathbf{r}, t)].\hat{\mathbf{s}}(\mathbf{r}), \tag{2.3}$$

which is a measurable quantity in experiments. Here, $\hat{\mathbf{s}}$ is the unit vector normal to the surface at position $\mathbf{r}$ on the surface.

As already mentioned, photon diffusion in an opaque material has many similarities with diffusion of electrons inside metals. Therefore it is handy to point out a few equivalent quantities for these two systems. The optical transmittance of a non-absorbing opaque object in the diffusive regime is the equivalent to the electrical/thermal conductance in a piece of metal. The effusion function is equivalent to the electric/thermal current normal to the surfaces. A cavity in the opaque medium is the equivalent of a leaking capacitor in the electric circuit, a capacitor parallel to a resistor. Hundred percent reflectivity denotes a perfect capacitance.

2.1.3 Validity of photon diffusion theory

The non-dissipative photon diffusion has been shown to be highly predictive of the average distribution of quantities within the limits of two inequalities[15]

$$\lambda_0 \ll \ell \ll L, \tag{2.4}$$

where λ_0 is the wavelength of light in vacuum and L is the sample size. The first inequality avoids the effect of Anderson localization. The second inequality reflects the presence of substantive diffusive region inside the skin layer so that the diffusive quantities overcome the single-scattering contribution. For practical reasons it is good to have low absorption $L \ll L_a$, where L_a is the absorption length. As far as $\ell \ll L_a$ the absorption contributions can all be incorporated by adding an absorption term, proportional to the energy density, to the left hand side of equation (2.2). But presence of absorption can hinder a lot of interesting phenomena that can happen in the diffusive regime and on the limit of transition to the localized regime.

From the observational point of view the photon diffusion equation can predict various quantities down to mesoscopic scales; i.e. a few mean free paths. For quantities which are varying at smaller scales, a full consideration of the Maxwell's equations is needed. In solid-state opaque objects the scatterers are often comparable to the wavelength in size, which may show up in various resonance effects[16]. Except for their averaged representatives, the precise shapes and positions of the scatterers often are not known and are not relevant in mesoscopic or macroscopic quantities. Reminding the behavior of light waves in the skin layer, I emphasize the ambiguity of diffusive behavior, and therefore impreciseness of photon diffusion solution, near the interfaces of the opaque material.

Refereing back to the resemblance of photon diffusion and electrical conductance in metals[17], the equivalent for light wavelength in the electronic system is the de Broglie wavelength of electrons, which is very much dependent on the effective mass of electrons in the bulk material. A typical mean free path for electron scattering in a metal element like copper is roughly 40 nm. The application of electron diffusion theory in bulk metal results in Ohm's law. The Ohm's law is not correct for very thin layers of metal[18].

2.2 Stationary regime

When the photon source is continuous in time, the solution to the photon diffusion equation (2.2) lies in the stationary regime at moments after the Thouless time, $t_s = L^2/D$. In more precise words, the variation of average energy density, the solution to equation (2.2), over time is less than the microscopic fluctuations of the exact energy density for a given realization of scatterers. The stationary diffusion regime also holds when the sources are pulsed with a pulse duration that is much longer than t_s assuming that the intensity envelope is smooth.

2.2.1 Poisson equation

In the stationary regime the time derivative of energy density distribution is zero. Equation (2.2) is then reduced to

$$\nabla^2 u(\mathbf{r}) = -\frac{S(\mathbf{r})}{D} \tag{2.5}$$

that is very well known as the Poisson equation. This form of Poisson equation also dictates the electrostatic potential, $\phi(\mathbf{r})$, in vacuum and dielectrics, as well as the current distribution in conductors when neglecting the Faraday interaction. In electrostatics, the Poisson equation is often written as

$$\nabla^2 \phi(\mathbf{r}) = -\frac{\rho(\mathbf{r})}{\varepsilon}, \tag{2.6}$$

where $\rho(\mathbf{r})$ is the charge density distribution and ε is the electric permittivity of the medium. The concepts of superposition and uniqueness of solution can be applied to stationary diffusion solutions, like other linear differential equations. We may also use the method of images, a powerful tool for dealing with point sources and interfaces.

Here it is helpful to mention a few quantities which are equivalent in electrostatics and stationary photon diffusion in homogeneous media.

$$\begin{aligned} \text{electrostatics} &\longleftrightarrow \text{photon diffusion} \\ \varepsilon &\longleftrightarrow 1, \\ \phi(\mathbf{r}) &\longleftrightarrow D u(\mathbf{r}), \\ E_\perp(\mathbf{r}) &\longleftrightarrow I(\mathbf{r}), \\ \rho(\mathbf{r}) &\longleftrightarrow S(\mathbf{r}), \end{aligned} \tag{2.7}$$

where $E_\perp(\mathbf{r})$ is the component of the static electric field normal to the surface, and $S(\mathbf{r})$ denotes the fraction of the coherent incident beam that is converted to diffusive intensity at position $\mathbf{r}$. Use of this equivalence has been previously made to locate objects in opaque media[19].

2.2.2 Boundary conditions

The solution of Poisson equation, like other linear differential equations, is strongly dependent on the boundary conditions. As mentioned in the previous sections of this chapter, the photon diffusion equation is rather ambiguous near the interfaces of opaque object and free space. Exactly the same region dedicates the boundary conditions. In fact, in order to

bring the predictions closer to reality, most of the proposed corrections to the photon diffusion model deal with redefinition of the boundary conditions. The concept of extrapolation length is defined to count for the finite reflectivity of interfaces[20–22]. A more sophisticated theory, called Radiative transport theory, treats the interfaces more rigorously[15].

The source distribution of diffusive intensity is in fact extended. It is best described with a continuous function that is exponentially decaying over a length-scale of one mean free path inside the object[23]. A simplified model treats the source as a Dirac-delta function positioned one mean free path inside the material. In the analogy with electrostatics the Dirac-delta source function is an equivalent to a point charge.

In the rest of this chapter I assume the simplest assumptions. The results of the experiments presented in this thesis fall into two categories. For some of the samples/experiments the results can be described by photon diffusion and this simple assumptions, within the range of errors. Other cases violate the photon diffusion model, and even the more rigorous assumptions will not help.

My assumptions are as follows: Part of the incident beam on the object, which is not reflected due to index mismatch, turns into a Dirac-delta source of diffusive photons, exactly at a mean path distance from the interface. The diffusion equation can be applied to the whole bulk of opaque material and absorption is negligible. The surfaces are treated as perfect absorbers of diffusive photons which means that all the diffusive photons that reach the boundaries will couple out to propagating waves in the surrounding. The outgoing intensity is given by equation (2.3).

2.2.3 Method of images

As a handy tool for solving the Poisson equation, I'll frequently use the method of images in the rest of this chapter. What follows are a few rules in this method. Keeping in mind the equivalence with photon diffusion, I use the electrostatic expressions for this part.

The method of images (also known as the method of image charges and method of mirror charges) is a problem-solving tool. The name originates from the replacement of certain elements in the original layout with imaginary charges, which replicates the boundary conditions of the problem. It simplifies the problem with physical boundaries to a problem without boundaries using more number of charges. The applicability of the solution is a direct outcome of uniqueness theorem. Plane and spherical interfaces with constant potential next to point charges can be replaced by point charges of definite magnitude and position. Similar rules hold for line sources and cylindrical surfaces. In case of more than one interface, it is possible to include multiple or infinite number of images. The solution is only valid in a region that contains none of the image charges

2.2.4 Anisotropic diffusion

Due to birefringence or shape of the scatterers, an opaque medium may be anisotropic, but still homogeneous. Using a tensor instead of a number for the diffusion constant it is still possible to define a photon diffusion model that predicts correctly some of the mesoscopic quantities. The microscopic origin of diffusion tensor is not yet well understood.

A coordinate system orientation may be chosen such that diffusion tensor is diagonal,

i.e.

$$\bar{\mathbf{D}} = \begin{pmatrix} D_{xx} & 0 & 0 \\ 0 & D_{yy} & 0 \\ 0 & 0 & D_{zz} \end{pmatrix}. \tag{2.8}$$

In this case, the stationary and anisotropic photon diffusion equation reads

$$D_{xx}\frac{\partial^2}{\partial x^2}u(\mathbf{r}) + D_{yy}\frac{\partial^2}{\partial y^2}u(\mathbf{r}) + D_{zz}\frac{\partial^2}{\partial z^2}u(\mathbf{r}) = S(\mathbf{r}). \tag{2.9}$$

The formal Poisson equation can be obtained by scaling the coordinates.

$$\mathbf{r} = x\hat{\mathbf{x}} + y\hat{\mathbf{y}} + z\hat{\mathbf{z}} \longrightarrow \mathbf{r}' = \frac{x}{D_{xx}^{\frac{1}{2}}}\hat{\mathbf{x}}' + \frac{y}{D_{yy}^{\frac{1}{2}}}\hat{\mathbf{y}}' + \frac{z}{D_{zz}^{\frac{1}{2}}}\hat{\mathbf{z}}'. \tag{2.10}$$

$$\nabla'^2 u'(\mathbf{r}') = \frac{\partial^2}{\partial x'^2}u'(\mathbf{r}') + \frac{\partial^2}{\partial y'^2}u'(\mathbf{r}') + \frac{\partial^2}{\partial z'^2}u'(\mathbf{r}') = S'(\mathbf{r}'), \tag{2.11}$$

where $u'(\mathbf{r}')$ and $S'(\mathbf{r}')$ are the average energy density and source distribution defined in the scaled coordinates. Special care of scaling back to the original (lab) coordinates should be taken when comparing the prediction with experimental results.

2.3 Slab geometry

Unlike stellar extended masses, most opaque objects in solid state have well-defined interfaces. An opaque cube is a very simple and yet easily producible example. By slab geometry I refer to an extended diffusive region confined between two parallel plates. In practice, a thin layer of an opaque material attached to a flat substrate can be considered as an slab. Here we assume that the slab is surrounded by free space and light source is incident from outside. The slab thickness is denoted by L and the z-axis is assumed to be perpendicular to the slab interfaces.

2.3.1 Transmittance for plane wave

If an opaque slab is illuminated by a plane wave[3] perpendicular to the slab, the problem can be reduced to one dimension, due to transverse symmetry. The energy density is constant in the xy plane. Based on coordinates of figure 2.2, the photon diffusion equation (2.5) and the boundary conditions[4] can be written as

$$\frac{d^2u(z)}{dz^2} = \frac{I_0}{D}\delta(z-\ell), \tag{2.12}$$

$$u(0) = u(L) = 0. \tag{2.13}$$

[3] In experiment, a Guassian beam with a beam waist that is much larger than the thickness of the slab may be treated as a plane wave.

[4] Extensive research has been done on what boundary condition should be considered for an slab. The concept of extrapolation length z_e[20] conveys a lot of these boundary effects. After introducing this concept, many of the transmittance equations stay the same but only for the mean free path ℓ and thickness L of the slab which should be replace by an effective mean free path $\ell_e = \ell + z_e$ and an effective thickness $L_e = L + 2z_e$.

Here I_0 is the intensity of the incident light. The reflectivities of the interfaces are assumed to be zero. The solution $u(z)$ can be found by integrating equation (2.12) along the z-axis,

$$Du(z) = \begin{cases} I_0 \frac{(L-\ell)z}{L} & z \leqslant \ell, \\ I_0 \frac{(L-z)\ell}{L} & z > \ell. \end{cases} \tag{2.14}$$

The transmitted intensity through the opaque slab is found using equation (2.3). The transmittance of the slab is then the first derivative of $Du(z)$ at the second interface divided by the incident intensity;

$$T = \frac{\ell}{L} \tag{2.15}$$

for a plane wave normal to an opaque slab of thickness L.

2.3.2 Effusion from slab for point source

If an opaque slab is illuminated by a focused beam where the size of the focus is much smaller than the slab thickness, it can be approximated as a point source of diffusive photons, one mean free path inside the slab. Due to axial symmetry the parameters can most simply be described in cylindrical coordinates, as defined in figure 2.2. Here the method of images is very handy. The electrostatic equivalent is a positive point charge, Q, between two grounded planes (with zero potential). Infinite number of image charges must be considered. Summing the contribution of the point charge and all its images, the z-component of the electric field on the second interface can be written as

$$E_z(r,\theta,L) = \frac{1}{4\pi} \sum_{m=1}^{\infty} [\frac{2Q[(2m-1)L-\ell]}{(r^2+[(2m-1)L-\ell]^2)^{3/2}} - \frac{2Q[(2m-1)L+\ell]}{(r^2+[(2m-1)L+\ell]^2)^{3/2}}]. \tag{2.16}$$

As a result of the Guass theorem, the surface integral of the electric field over any closed surface is equal to the charge inside. As the whole intensity of light exiting the slab should be equal to the incident intensity, one can substitute the charge value, Q, with the incident power, P_0/D, and get the effusion function over the surface of the slab. The effusion function at the second interface up to the first order in ℓ/L reads

$$I(r,\theta,L) = \frac{P_0\ell}{\pi} \sum_{m=1}^{\infty} \frac{2(2m-1)^2L^2 - r^2}{[(2m-1)^2L^2 + r^2]^{5/2}}. \tag{2.17}$$

The plot of (2.17) resembles a bell with a rounded peak. Interestingly the shape of the bell does not depend on the mean free path, but only on the thickness of slab. The maximum effusion value and the radius which the effusion value falls to half of the maximum can be written as

$$I_{max} = \frac{7\,\zeta(3) P_0}{4\pi} \frac{\ell}{L^3}, \tag{2.18}$$

$$r_{(\frac{1}{2})} = \alpha L \quad (\alpha \simeq 0.55). \tag{2.19}$$

The function $\zeta(i)$ in equation (2.18) is the Riemann Zeta function. If the slab is anisotropic, assuming that the principle axes of anisotropy coincide with the defined coordinates, the shape of the hill is deformed along the axes. The equi-intensity contours are then elliptical.

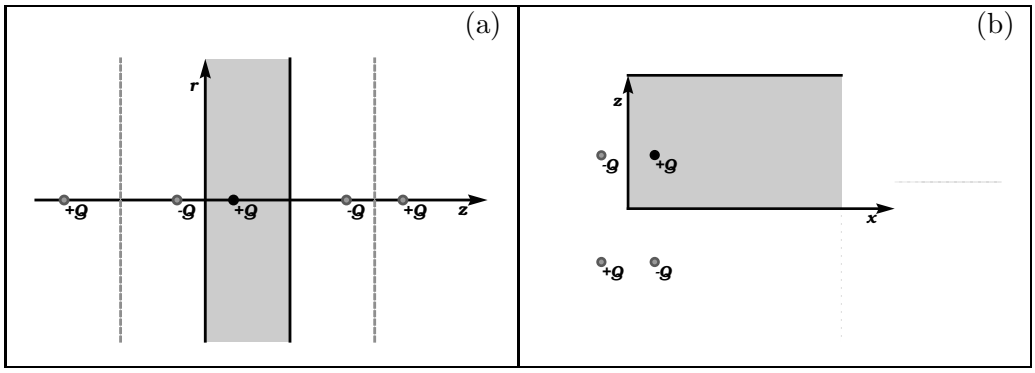

Figure 2.2: *A focused source of diffusive photons in opaque object is treated as equivalent to a point electric charge positioned one mean free path inside the sample.* (a) *or a slab geometry infinite number of mirror charges are required.* (b) *In a broken-slab geometry 3 mirror charges are sufficient if the effect of the other further boundaries is neglected.*

As discussed in section 2.2.4, we can derive the long and short diameters of the elliptical intensity contour at half the peak intensity;

$$r_{(\frac{1}{2})}|_{\theta=0} = \alpha(\frac{D_{xx}}{D_{zz}})^{\frac{1}{2}}L \tag{2.20a}$$

$$r_{(\frac{1}{2})}|_{\theta=\frac{\pi}{2}} = \alpha(\frac{D_{yy}}{D_{zz}})^{\frac{1}{2}}L \tag{2.20b}$$

The ratio between these two diameters can be used for measuring the anisotropy regardless of the thickness of the sample[24]. Also note that when $D_{xx} = D_{yy}$, although the distribution is axially symmetric, the width of the intensity distribution on the second interface may be used to define D_{xx}/D_{zz}.

2.4 Half-slab geometry

The breakdown of diffusive regime and onset of Anderson localization has been explored via experiments on a series of effectively infinite slabs of various thicknesses to conclude[10]. One experimental difficulty with this approach is that it is often hard to assure the bulk and surface properties of any two slabs of different thickness are identical. This uncertainty introduces large error on measurements due to variations in sample-dependent surface properties, variation in porosity from sample to sample, etc[25].

To address this difficulty, I propose use of half-slab geometries in which the observation interface is perpendicular to the illumination interface. I argue that this geometry allows more information regarding the energy distribution inside the slab to be determined. When illuminating with a focused source, the distance between the source and the observation interface can be varied in a single sample. This variation in separation serves a similar purpose to the variation in thickness in the infinite-slab geometry without requiring multiple samples. For anisotropic samples, the multiple available directions for illumination or detection provide additional information for understanding the underlying mechanism of anisotropic diffusion.

The half-slab geometry is shown in figure 2.2. In the following calculations, first we assume the sample thickness L to be infinitely large. We then describe quantitatively the

effect of finite thickness and the second interface, and the condition under which their effects are negligible.

2.4.1 Transverse effusion for a point source

First we assume incident beam is focused on the side of a thick broken-slab. In the language of electrostatics, a point charge Q is positioned at $\mathbf{r}_s = \ell\hat{\mathbf{x}} + z_s\hat{\mathbf{z}}$ in the Cartesian coordinates shown in figure 2.2, where z_s denotes the distance between the illumination spot and measuring interface. Considering $x = 0$ and $z = 0$ planes as zero potential surfaces, three image charges are needed to build up the solution to Poisson equation. We are interested in the effusion distribution on $z = 0$ plane, which I call transverse effusion function. The arrangement of point sources described in figure 2.2 yields the transverse effusion function

$$I^{\perp}(x, y, 0) = \frac{P_0}{2\pi}[\frac{z_s}{((x-\ell)^2 + y^2 + z_s^2)^{3/2}} - \frac{z_s}{((x+\ell)^2 + y^2 + z_s^2)^{3/2}}]. \tag{2.21}$$

Assuming $\ell \ll z_s$ and excluding higher orders of ℓ/z_s, equation (2.21) can be simplified to

$$I^{\perp}(x, y, 0) = \frac{3P_0\ell}{\pi}\frac{xz_s}{(x^2 + y^2 + z_s^2)^{5/2}}. \tag{2.22}$$

Similar to transmittance distribution the mean free path appears only in the prefactor. The shape of the function is dependent only on the distance of light source from the observation plane. It is useful to extract some simple parameters that describe the size and shape of the effusion function. Here I select the total effusion from cross section $T^{\perp}$, which is the integration of effusion function over the half-plane $[x > 0, z = 0)$ divided by incident intensity. The peak of effusion function $I^{\perp}_{max}$, the peak position x_{max}, and x_c, the first moment of x weighted by the effusion function, are also three interesting values that I consider. The integration will be easier in the cylindrical coordinates $\hat{\mathbf{r}} = \sin\theta\hat{\mathbf{x}} + \cos\theta\hat{\mathbf{y}}$. Here I summarize the results

$$x_{max} = \frac{z_s}{2}. \tag{2.23}$$

$$I^{\perp}_{max} = \frac{48P_0}{\pi 5^{5/2}}\frac{\ell}{z_s^3}. \tag{2.24}$$

$$T^{\perp} = \frac{3\ell}{\pi}\int_0^{\infty}\int_0^{\pi}\frac{rz_s\sin\theta}{(r^2 + z_s^2)^{5/2}} r\sin\theta\, d\theta\, dr = \frac{1}{2\pi}\frac{\ell}{z_s}. \tag{2.25}$$

$$x_c = \frac{1}{P_0 T^{\perp}}\int_0^{\infty}\int_{-\infty}^{\infty} xI^{\perp}(x, y, 0)\, dx\, dy = \frac{2z_s}{\pi}. \tag{2.26}$$

The second interface of the slab;

The presence of another interface at some distance from the source $z = L$, adds a bit to the complexity of the solution. In this case an infinite number of image charges should be considered. The calculation is straight-forward and here I plot, in figure 2.3, the relative correction resulted from the other images to the $I^{\perp}(z_s/2, 0, 0)$ versus the position of source. The correction due to images in the second interface is less than 3% when the source is located near the central point on the illuminated side of the slab.

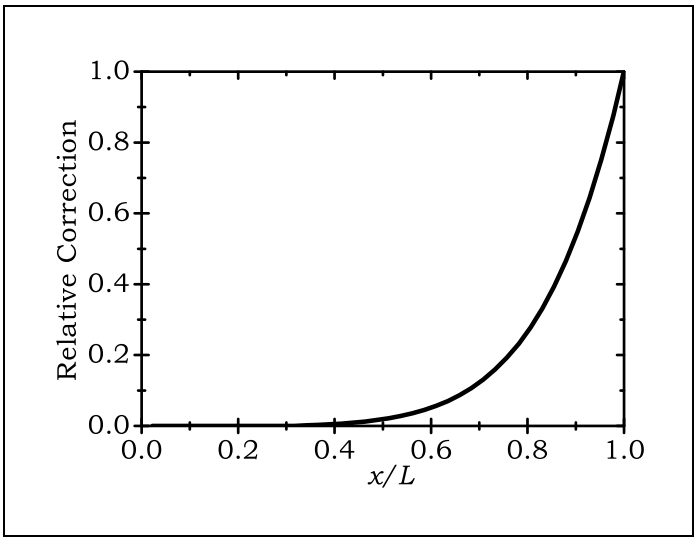

Figure 2.3: *The relative correction in peak of effusion intensity as presented by equation (2.24) after considering the infinite number of mirror charges due to the second interface (Assumption: $\ell = 0.1L$).*

2.5 Non-stationary regime

In this section we consider a pulsed source of pulse length d at a repetition rate of f. If the pulse duration is shorter than the Thouless time $t_s = L^2/D$, the solutions are not stationary and the diffusion equation should be solved in full.

2.5.1 General solution in slab geometry

As discussed in section 2.3.1 an opaque slab that is illuminated with an expanded beam can be treated by using a one-dimensional diffusion equation,

$$\frac{\partial}{\partial t}u(z,t) - D\frac{d^2}{dz^2}u(z,t) = S(z,t). \tag{2.27}$$

Using the boundary conditions $u(0,t) = u(L,t) = 0$, all the solutions for photon diffusion inside the slab of thickness L can be expanded in terms of a complete set of eigenfunctions

$$u_{m,t_0}(z,t) = \frac{2}{L}\sin(\frac{m\pi z}{L})\exp(\frac{-m^2\pi^2 D(t-t_0)}{L^2})\Theta(t-t_0), \tag{2.28}$$

where m is a positive integer number and t_0 is a real number. $\Theta(t-t_0)$ is the Heaviside step function which guaranties casuality.

We treat the problem of slab transmittance for an expanded beam in the non-stationary regime. The stationary solution was discussed in section 2.3.1. I assume the spatial pulse envelope in vacuum is a Guassian function with a width of d. The source of diffusive photons, which is located on a plane parallel to the interface $z = \ell$, reads

$$S(z,t) = \frac{I_0}{D}\delta(z-\ell)\Pi(t), \tag{2.29}$$

where $\Pi(t)$ is the normalized pulse-envelope function. Expanding the source distribution in terms of the eigenfunctions $u_{m,t_0}(z,t)$, and solving the photon diffusion equation yields

$$u(z,t) = \frac{I_0}{D}\sum_{m=1}^{\infty}\sin(\frac{m\pi\ell}{L})\int_0^{\infty}\Pi(t_0)u_{m,t_0}(z,t)dt_0. \tag{2.30}$$

For a sufficiently long pulse at times $t_s \ll t < d/c$, equation (2.30) will converge to the stationary solution, which is described in section 2.3.1.

2.6 Optical nonlinearity in opaque material

An opaque medium can also be optically nonlinear. This nonlinearity can be an intrinsic property of the micro-structure, the shape of the scatterers or a result of enormous interfacial area present in most opaque objects[5]. As the nonlinear conversion mechanism is microscopic, a full treatment of Maxwell's equations is needed in order to solve the problem in opaque materials. The generation of higher optical harmonics in strongly-scattering materials has not been fully understood, but some simplified models have been developed[26–30] that only serve as an approximation in the diffusive regime. In this thesis we consider only the case of optical second-harmonic generation.

2.6.1 Nonlinear mechanism for diffusive photons

In the simplest approximation, the source distribution of the second harmonic diffusive photons inside the opaque material, is a constant factor times the square of the energy density of the fundamental light

$$S^{(2)}(\mathbf{r},t) = \Gamma[u(z,t)]^2, \tag{2.31}$$

assuming absorbtion and down-conversion are negligible. All of the conversion mechanisms that depend on microscopic properties such as the nonlinear coefficient of the bulk of the material, its dispersion, and the geometry of the scatterers and the interfaces contribute to the effective nonlinear coefficient Γ. The conversion efficiency is assumed to be so low that the distribution of fundamental diffusive photons is not affected. The interaction of fundamental and second-harmonic diffusive photons which generates higher harmonics is also neglected.

A well-known effect in nonlinear optics is phase mismatch, which causes destructive interference between the fundamental and the second-harmonic beam after they co-propagate a path longer than a certain coherency length, $L_c(\omega) = \pi/|k(\omega) - k(2\omega)|$. Finite L_c is a result of dispersion $k(\omega) = k_0/n(\omega)$, where k_0 is the free-space wave number and $n(\omega)$ is the refractive index of the material. Phenomenological arguments indicate that Γ is linearly proportional to the mean free path ℓ if $\ell \ll L_c$ and reaches its maximum when $\ell \approx L_c$[29]. This dependency provides an internal ruler for measuring the mean free path deep inside the opaque material. It should be noted that use of such an internal probe of the mean free path would be entirely new, and contrasts strongly with the usual methods, which measure only the surface penetration depth.

[5]Second-order nonlinearity is absent in some non-crystalline materials or crystal structures because of symmetry. Relatively huge non-linearities may arise at the interfaces of these materials with others due to symmetry-breaking.

2.6.2 Stationary solution

For the slab illuminated with a continuous plane wave, the solution derived in section 2.3.1 can be used to write the diffusion equation for the second-harmonic photons,

$$\frac{d^2u^{(2)}(z)}{dz^2} = \Gamma[u(z)]^2. \tag{2.32}$$

Inserting the solution to the fundamental photon density distribution from equation (2.14) and taking care of the limits at interfaces, $u^{(2)}(0) = u^{(2)}(L) = 0$, equation (2.32) can readily be integrated yielding the second-harmonic energy distribution inside the slab:

$$u^{(2)}(z) = \frac{\Gamma I_0^2}{D^2} \times \begin{cases} \frac{\tilde{\ell}^2 z^4}{12L^2} + \frac{\ell^2\tilde{\ell}^2}{12L^3}[(\tilde{\ell}-\ell)\tilde{\ell} - \frac{\ell^2+\tilde{\ell}^2}{4}]z & z \leqslant \ell \\ -\frac{\ell^2\tilde{z}^4}{12L^2} + \frac{\ell^2\tilde{\ell}^2}{12L^3}[(\tilde{\ell}-\ell)\ell + \frac{\ell^2+\tilde{\ell}^2}{4}]\tilde{z} & z > \ell \end{cases} \tag{2.33}$$

Here, $\tilde{z} = L - z$ and $\tilde{\ell} = L - l$. Note that $u^{(2)}(z)$ is invariant over $[z \leftrightarrow \tilde{z},\ \ell \leftrightarrow \tilde{\ell}]$ interchange. A plot of this energy distribution is shown in figure 2.4. This plot is very similar to the plot of Makeev and Skipetrov[28]. Their derivation is identical to mine except that they position the source of diffusive photons at $z = 0$.

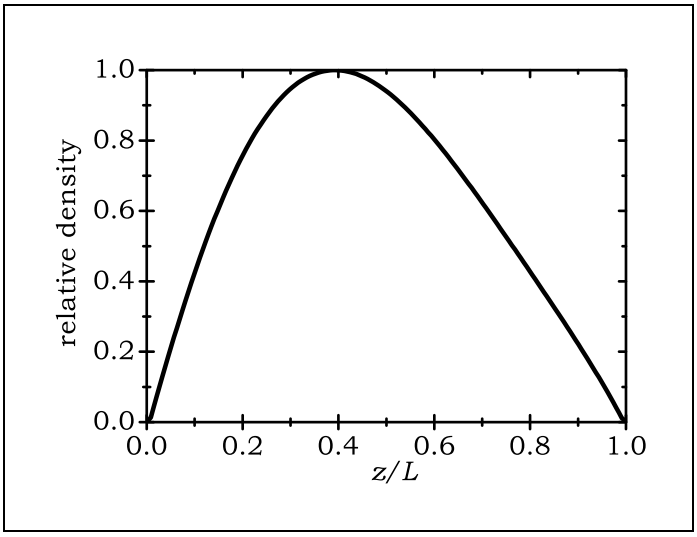

Figure 2.4: *Distribution of second-harmonic photons inside an opaque slab in the stationary regime for* $\ell = 0.1L$.

2.6.3 Non-stationary solution

In the non-stationary regime, the second-harmonic photons follow the non-stationary diffusion equation. Setting the source distribution defined in equation (2.31) the diffusion equation for second-harmonic photons in a slab reads

$$\frac{\partial}{\partial t}u^{(2)}(z,t) - D^{(2)}\frac{d^2}{dz^2}u^{(2)}(z,t) = \Gamma[u(z,t)]^2, \tag{2.34}$$

in which $u(z,t)$ can be determined from equation (2.30). It is an straight-forward calculation to expand the right hand side in terms of relevant eigenfunctions similar to what was defined

in equation (2.28). Applying the usual boundary conditions, $u^{(2)}(0,t) = u^{(2)}(L,t) = 0$, the distribution of second-harmonic photons reads

$$u^{(2)}(z,t) = \frac{16\Gamma I_0^2}{L^3 D^2} \sum_{q=1}^{\infty}\sum_{p=1}^{\infty}\sum_{m=1}^{\infty}[\frac{mpq[1-(-1)^{m+p+q}]}{m^4+p^4+q^4-2(m^2p^2+p^2q^2+m^2q^2)} \times \sin(\frac{m\pi z}{L})\sin(\frac{p\pi \ell}{L})\sin(\frac{q\pi \ell}{L}) \times \int_{-\infty}^{t} \exp(\frac{-m^2\pi^2 D^{(2)}(t-t_0)}{L^2})\Pi_{p,t_0}\Pi_{q,t_0}dt_0]. \tag{2.35}$$

where Π_{p,t_0} is the pulse envelope projected onto the time-dependent part of the eigenfunction $u_{p,t_0}(z,t)$, which can be formulated as

$$\Pi_{p,t_0} = \int_{-\infty}^{t_0} \Pi(t)\exp(\frac{-p^2\pi^2 D(t_0-t)}{L^2})dt. \tag{2.36}$$

The transmitted and reflected intensities at any moment are proportional to spatial derivatives of $u^{(2)}(0,t)$ and $u^{(2)}(L,t)$ respectively. As, practically, very fast measurements are difficult, the measured quantity is usually the accumulated energy over one pulse duration. Disregarding the prefactor in equation (2.35) the the accumulated energy distribution inside an slab is plotted in figure 2.5(a) for different values of mean free path at a constant pulse length $d = L$. I hereby define

$$R^{(2)} = \frac{D^{(2)}}{I_0^2}\int_{-\infty}^{\infty} \frac{\partial u^{(2)}(z,t)}{\partial z}|_{z=0}\, dt, \tag{2.37a}$$

$$T^{(2)} = \frac{D^{(2)}}{I_0^2}\int_{-\infty}^{\infty} \frac{\partial u^{(2)}(z,t)}{\partial z}|_{z=L}\, dt \tag{2.37b}$$

as the average efficiency per unit area of second-harmonic generation and coupling into propagating waves in the backward and forward directions, respectively. These factors can be measured from the averaged power of radiated second-harmonic light integrated over 2π solid angle and divided by the square of the incident power of fundamental light. It is worth mentioning that although $R^{(2)}$ and $T^{(2)}$ both depend on the conversion efficiency Γ the sample thickness L and the diffusion constant D, their ratio is independent of Γ and depends on L and D only in form of dimensionless variables ℓ/L and d/L, where d is the pulse length. Therefore, stating the results in terms of $\eta = R^{(2)}/T^{(2)}$ will be an instructive way of comparing diffusive properties of different samples independent of their size and effective nonlinear coefficient. For the stationary solution derived in section 2.6.2 this ratio is always a constant equal to 3 on the condition that the slab is optically thick ($\ell/L \ll 1$). Previously, de Boer *et al.* found the same result for stationary regime using rigorous calculations[30]. Finally I emphasize that in the measurement of nonlinear efficiency, although accumulated intensities are measured, dynamic parameters can also be determined unlike the linear measurements.

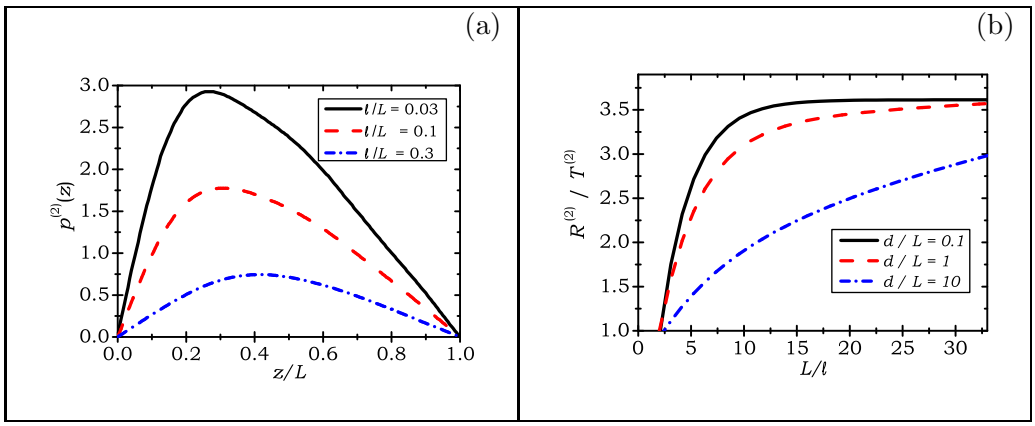

Figure 2.5: (a) *Accumulated energy distribution of second-harmonic photons inside an opaque slab in the non-stationary regime for 3 different mean free paths at a vacuum pulse length of* $d = 0.1L$. (b) *Ratio of radiated second-harmonic light in the backward and forward direction,* $R^{(2)}/T^{(2)}$, *as a function of mean free path for 3 different pulse length.*

CHAPTER 3

Nano-porous GaP

In this chapter we address the fabrication process and a few properties of our samples.

3.1 History of GaP sponges

GaP sponges are made by anodic electrochemical etching a GaP wafer. By setting certain etching conditions[31] an interconnected complex network of pores, with pore sizes of about 150 nm can form inside the bulk. This process converts the transparent crystalline wafer into an opaque slab of porous GaP. The voltage, the chemical composition of the etching fluid, the doping concentration of the wafer, and the etching time affect the thickness of the sample, the pore size, and the air/GaP volume fraction. However, variations of up to few ten percent have been observed from sample to sample even when all the controllable conditions are set the same[36].

Different methods have been introduced to remove a layer from the top, because the porous structure on the surface of etched wafer is different from the bulk. These methods include photo anodic etching[32], chemical etching[33] and removing top layer after mid-way oxidization[34].

Porous GaP is of particular interest as it has been shown to be extremely strongly scattering. Schuurmans *et al* reported very short mean free path of $0.17 \pm 0.02\,\mu$m at vacuum wavelength $\lambda_0 = 685$nm[32] in a set of 10 samples at various thicknesses. Although the total transmission measurements showed a good agreement with diffusion theory prediction, the enhanced backscattering measurements showed signs of transition into Anderson localization regime[35]. The different results of these two experiments is not yet clear, but it was shown that absorption cannot explain the difference. Many efforts has been made to decrease the mean free path in these kind of GaP sponges [33, 36, 37] but none of them have achieved the low record which was set in 1999 by Schuurmans *et al*.

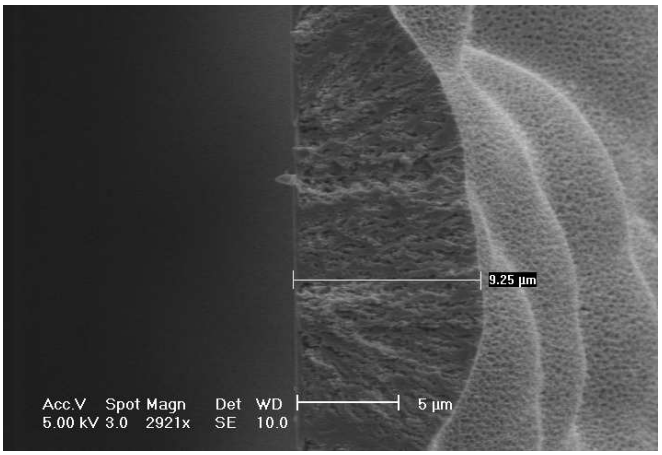

Figure 3.1: *Scanning electron micrograph of the removed top layer of a sample that has experienced a short oxidization period during the etching process. The left side is the polished surface of the GaP wafer and the right side is formed by the etching process before oxidization. The surface pattern on the right side is complementary to the surface of the investigated sample.*

Three new samples were made during this project[1]. These samples were subjected to a number of experimental probes, together with a selected set of previously fabricated GaP sponges[2].

3.2 Fabrication procedure

Our porous-GaP samples are made out of commercially available single crystal n-type gallium phosphide wafers. These wafers are doped with donor atoms in a density range of 2-20$\times 10^{17}$ cm^{-3}. The first etching process is generally the same for all the samples. A 9×9 mm^2 piece of GaP wafer is anodically etched under controlled electromotive force. The electric current is recorded in time. The total charge transported in the process is proportional to the amount of removed material, thus it allows calculation of the porosity for a known sample thickness. Different post-etching processes can be used to remove the top layer; to improve optical characterization, or increase the pore-size. As the pore size approaches the probing wavelength, the scattering strength of the sponge grows. In the past, the applied post-etching processes have been very different for each sample. This information is available in the COPS sample database, or the log-book of the person who has fabricated the sample. Further details about the samples fabricated in the past are not addressed in this thesis.

In the three new samples made during this project no post-etching procedure was applied. Instead, and oxidation step was added during etching to remove the top-layer. This step involves increasing the applied potential for a short period of time during etching, to create a thin layer of oxide which is more fragile than the rest of GaP sponge. After this step, etching is continued at the normal potential to produce the desired thickness

[1] Made by D.A. Mazurenko and R.G.W. Tjerkstra in the group of Complex Photonic Systems at University of Twente.

[2] All the samples now belong to the group of Photon Scattering at FOM Institute for Atomic and Molecular Physics, Amsterdam.

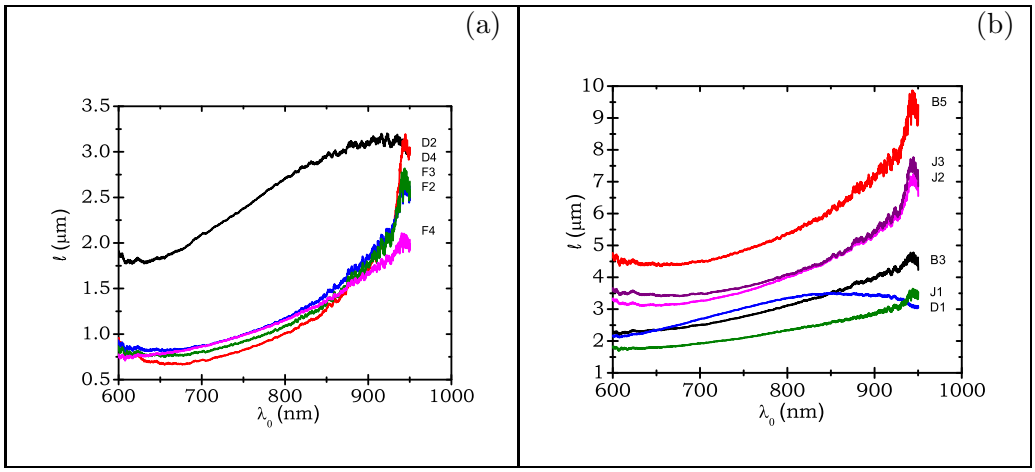

Figure 3.2: *Dependence of mean free path on probing wavelength is extracted from total transmission measurements.* (a) *group of stronger scattering samples* (b) *group of weaker scattering samples.*

of the porous layer. The first porous layer can later be carefully removed with tweezers. The bottom porous layer retains a wavy surface of about 2 μm in roughness, but has a porous structure similar to the bulk of the sponge. A scanning electron micrograph from the surface of this sample is shown in figure 3.1.

3.3 Sample characterization

There are various methods that can provide information about the structural and optical properties of the GaP sponges. Unfortunately, most of these methods are more sensitive to the surface properties of the sample than to its bulk properties. For this research scanning electron microscopy(SEM) is used for measuring the thickness of the porous layer and quantifying the average pore size. The refractive index of bulk GaP is taken from the literature[38, 39] and the porosity is used to calculate the effective refractive index of the sponges. Measurement of enhanced backscattering (EBS)[3] at 633 nm and total transmission at the whole range of visible light provided the information regarding the value and wavelength dependence of the mean free path in each sample (see figure 3.2). An EBS setup using a CCD detector and a total transmission setup using an integrating-sphere and a spectrum analyzer were specially made for these purposes. The specifications of these setups are presented in the appendices.

3.3.1 Quantifying pore size

High resolution scanning electron micrographs(SEM) reveal the nanometer-scale structure of the porous GaP sponges. From these images, it is possible to estimate the average pore size in the sponge. An standard way of quantifying the size scale of the pores from the SEM image is to calculate the auto-correlation of the image intensity for nearby points. This auto-correlation function is defined as

$$C_{\hat{\mathbf{x}}}(\delta x) = \frac{< B(\mathbf{r} + \delta x \hat{\mathbf{x}}) B(\mathbf{r}) >_{\mathbf{r}}}{< B(\mathbf{r})^2 >_{\mathbf{r}}}, \tag{3.1}$$

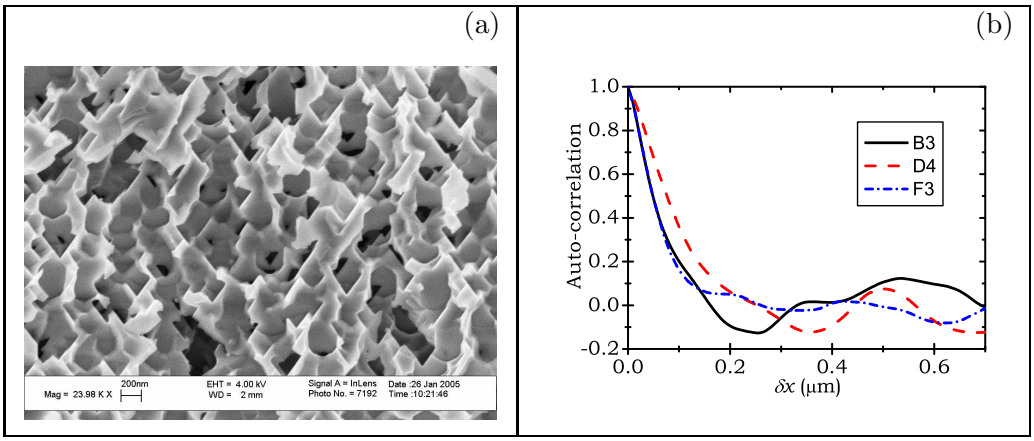

Figure 3.3: (a)*A typical scanning electron micrograph of GaP sponges, Courtesy of B. Bret.* (b) *Extracted auto-correlation for two of the stronger samples and one of the weaker samples*

where $B(\mathbf{r})$ is the difference between the brightness at position $\mathbf{r}$ on the image and the average brightness of the image. The symbol $<>_{\mathbf{r}}$ indicates averaging over the whole image (excluding near the boundaries). In principle, it is possible to measure the auto-correlation function for any direction. The dependence of $C_{\hat{\mathbf{x}}}(\delta x)$ on the direction $\hat{x}$ indicates the degree of anisotropy in the shape or distribution of the grains. In a granular image the auto-correlation decays from its peak at 1 at a rate that is proportional to the grain size. The extracted auto-correlation for 3 samples is shown in figure 3.2

3.3.2 Summary of properties for investigated samples

A summary of the most important properties of the investigated samples is prepared in table 3.1. The thicknesses are measured from SEM images. The mean free path values are determined using the total transmission setup and the EBS setup. For the details of these setups please look at the appendices.

Tag	Thickness (μm)	$\ell_1(\mu\text{m})$	$\ell_2(\mu\text{m})$	ℓ_2/ℓ_1	$k\ell$	E_f	V_e ($Volts$)	DB label
B3	63 ± 1	2.60 ± 0.13	6.25 ± 0.31	2.40	13.62 ± 0.18	1.71 ± 0.01	10.50	T020903-a
B5	116 ± 3	4.46 ± 0.22	11.98 ± 0.60	2.69	12.92 ± 0.14	1.56 ± 0.01	10.00	T230902
D1	32 ± 1	2.33 ± 0.12	5.66 ± 0.28	2.43	34.22 ± 0.84	1.54 ± 0.01	22.50	DmitryA2
D2	51 ± 2	1.69 ± 0.08	4.70 ± 0.23	2.79	20.63 ± 0.35	1.61 ± 0.01	22.50	DmitryB2
D4	43 ± 2	0.55 ± 0.03	2.27 ± 0.11	4.13	5.45 ± 0.10	1.75 ± 0.01	22.50	DmitryD2
F1	7.3 ± 1	0.48 ± 0.02	2.38 ± 0.12	5.00	$--$	$--$	14.70	S21051
F2	35.5 ± 1	0.75 ± 0.04	5.84 ± 0.29	7.81	4.48 ± 0.09	1.92 ± 0.01	14.70	S19052
F3	47.5 ± 1	0.57 ± 0.03	5.86 ± 0.29	10.27	4.57 ± 0.09	1.94 ± 0.01	14.70	S19053
F4	23.5 ± 1	0.74 ± 0.04	4.74 ± 0.24	6.43	3.92 ± 0.10	1.97 ± 0.02	14.70	S19054
J1	26 ± 1	1.70 ± 0.08	3.64 ± 0.18	2.14	10.73 ± 0.17	1.73 ± 0.01	11.20	S0603-1
J2	83 ± 3	3.09 ± 0.15	7.48 ± 0.37	2.42	13.91 ± 0.12	1.59 ± 0.01	10.00	S2003-1
J3	126 ± 4	3.49 ± 0.17	9.62 ± 0.48	2.76	7.50 ± 0.07	1.61 ± 0.01	15.00	S2303-1
U1	26 ± 1	0.81 ± 0.04	2.11 ± 0.11	2.62	3.82 ± 0.08	2.00 ± 0.02	–	?
U2	13 ± 1	1.34 ± 0.07	3.58 ± 0.18	2.67	6.69 ± 0.24	1.99 ± 0.02	–	?

Table 3.1: *Summary of specifications for the samples that are analyzed in this thesis. Hereafter samples will be referred to by their tags given in the first column. The thickness of the sponge is derived from scanning electron micrographs. The mean free paths ℓ_1 and ℓ_2 are measured for vacuum wavelengths of 650 nm and 1300 nm based on total transmission. Estimation of $k\ell$ is based on enhanced backscattering measurements at vacuum wavelength of 633 nm. E_f indicates the measured enhancement factor in the backward direction on the EBS curve. V_e is the applied electromotive force during etching process. DB label is the corresponding label of each sample in the COPS sample database.*

CHAPTER 4

Stationary effusion pattern

In this chapter I introduce two new experiments that can provide information on anisotropic diffusion in opaque slabs. In the case of less strongly scattering samples, very good agreement with the photon diffusion theory presented in chapter 2 is achieved. A comprehensive optical method is thus proposed for measuring optical anisotropy in all directions for a thin slab. In a set of more strongly scattering samples, behavior contradicting the diffusion-theory predictions is observed. I argue that these results may indicate real time observation of Anderson localization of light in strongly scattering media.

4.1 Introduction

Measuring the total transmission of light through an opaque slab has been used for many years as a means of determining the mean free path. In most of these experiments, an extended beam with a beam waist much larger than the sample thickness illuminates the sample. Such a measurement on a series of otherwise identical samples of varying thickness can be used to determine the mean free path. However, focusing the incident beam sharply on one side and measuring the intensity distribution at the other boundaries of the slab may provide more information about the scattering properties of the sample.

In this chapter I introduce two experiments . In the first experiment the beam is sharply focused on the back side of the sample and the effusion function at the front side is measured under a microscope. I refer to this experiment as transmittance microscopy. In the second experiment the opaque slab is broken so that its cross section is accessible. The beam is then sharply focused on the cross section of the sample and an orthogonal side is imaged. Thus the distance between the focus spot and the imaging plane can be varied. Varying this distance is in some ways similar to varying the thickness of the slab in the total transmission experiments. However, this parameter is in a single sample, thus eliminating the need for multiple samples and the problems associated with sample-to-sample variations. This approach may provide added sensitivity to effects such as Anderson localization. For

further reference I call the second type of experiment transverse effusion microscopy. I show that both experiments can be also useful in measuring the anisotropic diffusion inside the slab.

4.2 Diffusion of a focused beam in slab

A beam that is tightly focused on the surface of an opaque object can be modeled as an isotropic point source of diffusive photons positioned one mean free path from the surface inside the sample. Here the condition for tight focusing is that the focus size is much smaller than the thickness and size of the slab. Under these conditions, the equations derived in section 2.3.2 can be used to extract diffusive properties of the sample.

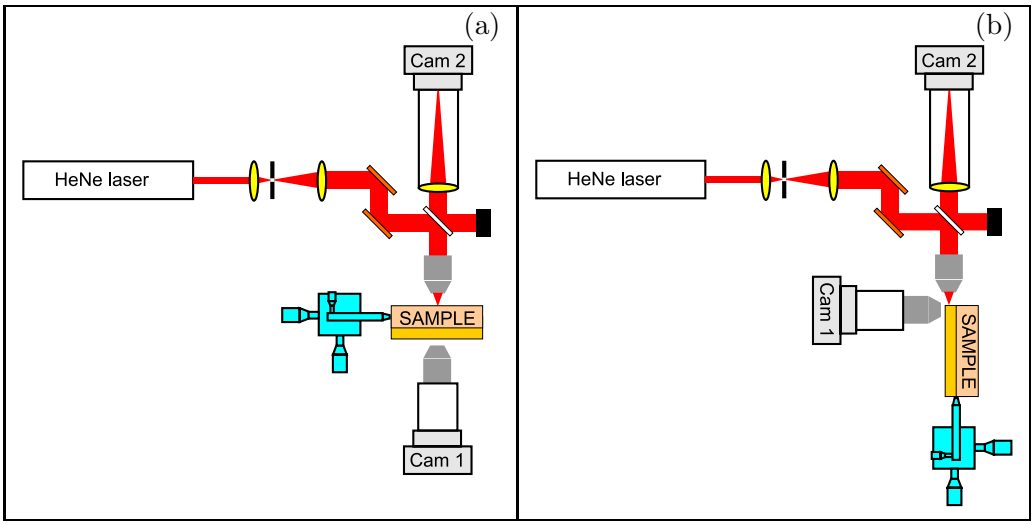

Figure 4.1: *Schematic views of the experimental setups for stationary measurements.* (a) *The transmittance microscopy setup focuses an expanded laser beam on the sample attached to the holder finger of a mechanical stage with three translational and two rotational degrees of freedom. A microscope objective images the opposite side of the sample and Cam 1 records the magnified intensity distribution. Cam 2 uses the focusing objective to image the incidence side of the sample.* (b) *The transverse effusion microscopy setup is similar to the transmittance setup except for the imaging part which is aimed perpendicular to the incidence direction.*

4.2.1 Transmittance microscopy setup

In the transmittance microscopy setup, the beam is focused on one interface of the opaque slab, and the surface distribution of the transmitted intensity, namely the effusion function, is recorded at the opposite interface. The experimental setup is schematically sketched in figure 4.1(a). Two lenses with a pinhole in between are used to expand the beam and filter spatial modes higher than the zero order. By use of a Peleco beam-splitter the surface of sample can be imaged using the same objective that focuses the laser beam on the sample. The size of focus spot is $\sim 3\,\mu$m and the field of view is $\sim 300\,\mu$m. This view is also helpful for alignment purposes. The focusing objective (10x 0.25NA) is fixed on a translation stage. The imaging objective (40x 0.65NA) is fixed on the camera using a tube to produce a magnification of 25 times. The sample is positioned between the two

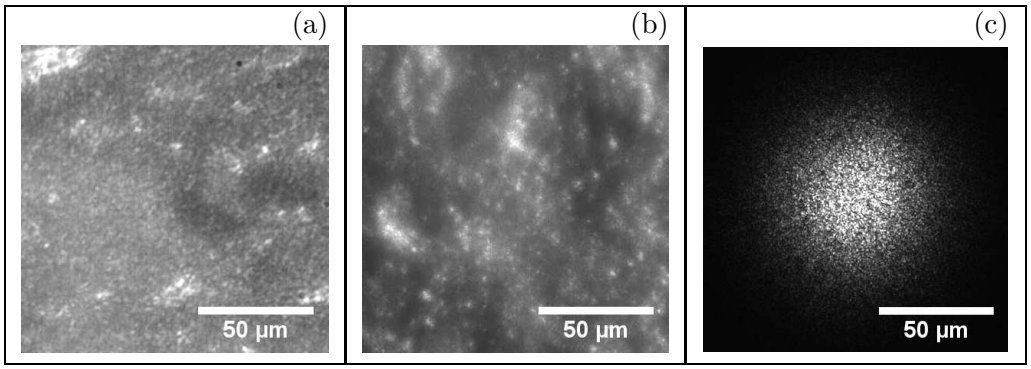

Figure 4.2: *Three images are captured for each transmittance pattern measurement. A measurement on sample F3 is presented here as an example.* (a)*Ambient light micrograph of the first interface imaged through the substrate.* (b)*Ambient light micrograph of the second interface .* (c)*Intensity distribution on the second interface (referred to as the transmittance pattern) while the laser beam is focused on the first interface.*

objectives attached to the finger of a manual translation stage. Cam 1, used for imaging the transmission pattern, is a solid-state cooled low noise Andor Ixon EMCCD camera with 1004×1002 pixels. Cam 2 is supplied by Mightex and uses a CMOS detection chip. Both cameras are controlled by the same computer.

After properly aligning all the components, a single measurement procedure consists of recording three images. First the laser beam is blocked and the porous GaP sample is placed between the objective with the substrate facing the incident beam. The GaP substrate is transparent so it is possible to focus on the etched part through the substrate. The distances are set such that each camera shows a sharp image from one surface of the etched part of the sample when illuminated with ambient light. The image at each camera is recorded under ambient light. The the ambient light is turned off and the laser block is removed and the magnified image of the intensity distribution pattern at the surface of the porous layer is recorded. The three images from a single measurements are shown in figure 4.2.

4.2.2 Extracting the mean free path

Similar to total transmission experiments, it is possible to extract the mean free path ℓ from transmittance microscopy measurements on a series of samples with similar scattering properties and different thicknesses based on the argument presented in section 2.3.2. Integrating the detected intensity over the whole image yields a quantity proportional to the total transmittance. The proportionality factor is an attribute of the detection components, the incident light intensity, and the surface properties of the sample. Here this factor is assumed to be sample independent for a given series. For extracting the absolute transmittance, a calibration measurement can be performed using a reference sample for which the mean free path is known from other measurements. As illustrated in equation (2.17) the intensity decreases as $1/r^3$ where r is the distance from the center of image, imposing a good convergence while integrating the intensity over the surface.

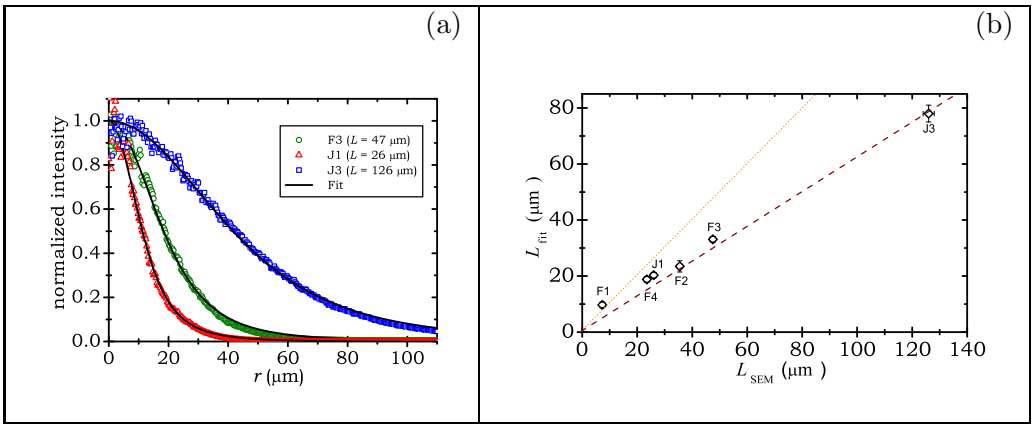

Figure 4.3: (a)*Symbols denote the axially averaged signal from the transmittance pattern measurement on different samples. Solid lines denote the fit to the prediction of diffusion theory, equation (2.17). The thickness of the slab and a normalizing coefficient are the two fitting parameters.* (b)*The thickness extracted from the fit illustrated in* (a) *is plotted versus the actual thickness measured based on scanning electron micrographs. The dotted line shows where the two quantities are equal. The dashed line is guided through the measurements points to address the systematic deviation related to the anisotropic diffusion in this group of GaP sponges.*

4.2.3 Extracting the anisotropy

Equation (2.17) describes the theoretical prediction for effusion function. The mean free path appears only in the prefactor, while the rest of the function depends only on the slab thickness. The axial symmetry of the recorded transmittance pattern is evident in most of the analyzed samples. To average out the speckle pattern, an axial averaging around the center is applied before fitting the measurements to equation (2.17). Here the fitting parameters are the sample thickness and the prefactor. Except for a few of the thinner samples, $L < 10$ μm, an excellent agreement between the measurement and the fit to the prediction of diffusion theory is observed. Several examples are illustrated in figure 4.3(a). Despite the match between the theory curve and data, the extracted thickness of the samples systematically deviates from the actual value, measured using scanning electron microscope. Inhomogeneities in the scattering strength, the surface effects and extrapolation length, or the diffusion being anisotropic are a few hypotheses that can be proposed to describe this deviation. The inhomogeneities must show their effect in scrambling the axial symmetry of the measured effusion pattern. This effect is also dependent on the measurement position of the sample. No such position dependence in the effusion pattern is observed during translating the illumination spot and the effusion patterns are always symmetric within 5%.

The systematic difference between the extracted slab thickness and the actual value is more than 30%. The best explanation for this deviation is that the diffusion of light inside the slab is anisotropic, as the anisotropic diffusion, effectively, re-scales the measured effusion pattern. From the discussion in section 2.2.4 and section 2.3.2, we know that the general pattern does not change but only re-scales itself. As the observed patterns are axially symmetric, we conclude that the anisotropy is uniaxial parallel to $\hat{\mathbf{z}}$. The fact that the effective thickness L_{fit} and actual thickness L_{SEM} maintain a linear dependence for different samples suggest that a single degree of anisotropy D_{zz}/D_{xx} can describe the systematic

deviation for all samples. We can thus related the optical anisotropy to same fundamental aspect of anodic etching of GaP. Using the slope of the line fitted to measured points in figure 4.3(b) and equation (2.20a), the ratio between diffusion constants in anodically etched GaP can be deduced:

$$\frac{D_{zz}}{D_{xx}} = \frac{D_{zz}}{D_{yy}} = 2.6 \pm 0.2 \; . \tag{4.1}$$

It is known that the pore in GaP sponges are structurally anisotropic when etched at a high etching potential[24]. However, it has previously been assumed that the samples that I analyzed were optically isotropic[32]. In the same report the average pore shape was quantitatively extracted and found anisotropic from the correlation function derivations on scanning electron micrographs. To our knowledge, this is the first time that uniaxial anisotropy perpendicular to the slab extension has been measured by optical methods in a thin slab of a few tens of micrometer.

4.2.4 Spatial spikes in effusion function

In this section I describe an anomalous axially non-symmetric effusion function observed for relatively thin samples, $L < 10$ μm. This pattern is characterized by unusual radial *spikes* as seen in figure 4.4(a). These samples are optically very thick, $L/\ell > 10$. Despite the presence of the unusual spikes, the axially averaged pattern is still similar to the bell shape distribution of the thicker samples. In order to characterize this unusual intensity distribution, it is useful to transform the image as

$$I(r,\theta) \rightarrow \frac{I(r,\theta) - < I(r,\theta) >_\theta}{< I(r,\theta) >_\theta}. \tag{4.2}$$

The result of this transformation is shown in figure 4.4(b). Axial correlation function can reveal the periodicity or self-similarity of the pattern. This function is plotted in figure 4.4(d) for various radii from the center of the image. The patterns are not periodic but exhibit self-similarity with a characteristic length-scale that is decreasing as it is measured further from the center, i.e. the structure is getting finer. This behavior is similar to a fractal but the exact origin of such a pattern in this kind of experiment is not yet understood.

4.3 Transverse effusion from half-slabs

Measurements on opaque slabs can reveal information regarding their mean free path and anisotropic diffusive properties. Furthermore, deviation from the diffusion regime toward the Anderson localization can be detected from measurements on a set of samples with different thicknesses[10, 32, 40]. I propose using half-slabs and measuring the effused light on an interface that is orthogonal to incidence interface. This method is useful for measuring diffusive and non-diffusive properties in a single sample. In this method, using a focused beam, it is possible to vary the separation between the diffusive-photons source and the measuring plane in a single sample. Recently this method has been experimentally tested in rectangular parallelepiped of white paint, and a good agreement with the diffusion theory has been demonstrated[41]. While, extracting mean free path and anisotropy is possible in this method, here I mainly focus on the cases which non-diffusive behavior is evident.

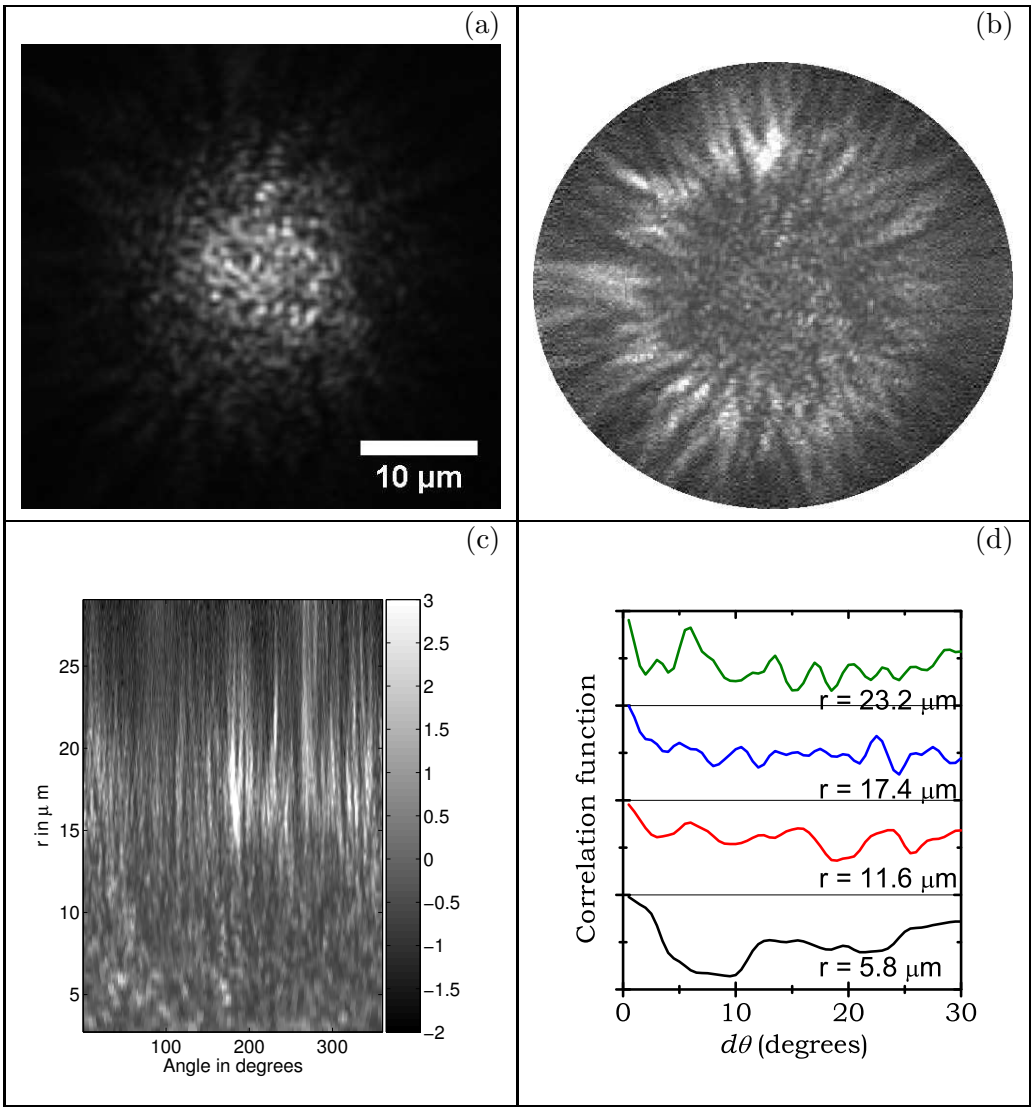

Figure 4.4: (a) *Effusion function for sample F1 ($L = 7.3$ µm) shows anomalous radial spikes.* (b) *The pattern shown in* (a) *is subtracted from and divided to the average envelope of the intensity to enhance the visibility of the spikes.* (c) *The pattern of* (b) *is mapped onto the flattened radius-angle coordinate system.* (d) *The brightness correlation function is extracted from* (a) *at various radii to quantify the possible periodicity or self-similar pattern.*

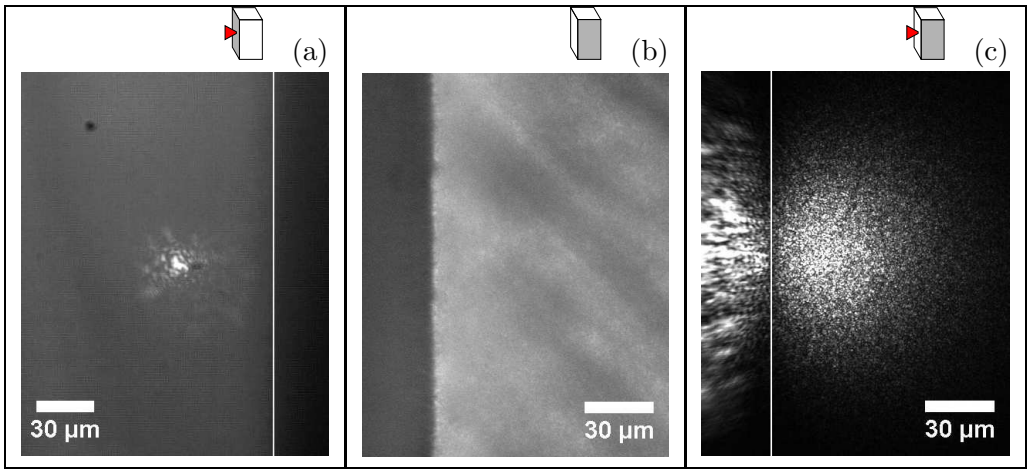

Figure 4.5: *Three images are captured for each transverse effusion function measurement. A measurement on sample J3 is presented here as an example.* (a)*Ambient light micrograph of the slab section imaged while the focused incident beam is illuminating the sample.* (b)*Ambient light micrograph of the top interface of the sample.* (c)*Intensity distribution on the top interface while the laser beam is focused on the side section (referred to as the effusion function). The vertical white line indicates the edge of the sample. The pattern on the left of the white line is the out of focus image of the backward reflection from the illumination spot. This light will not affect the actual pattern on the right because there these rays are blocked by the edge of the sample.*

4.3.1 Transverse effusion microscopy setup

The setup used for measuring the effusion function on side of the samples, the so called transverse effusion pattern, is similar to the transmittance microscopy setup already described in 4.2.1. The only difference is in the imaging section. In the transverse effusion microscopy setup, Cam 1 and the attached microscope objective are aimed orthogonal to the incident beam direction as shown in figure 4.1(b). Cam 2 in this setup is used both for imaging the illuminated side of sample and for measuring the position of the focussed light relative to the edge which is in the view of both cameras. An example of a set of three images that form a single measurement are shown in figure 4.5.

4.3.2 Deviation from the diffusive regime

It was shown in section 2.4.1 that in diffusive regime the total transverse effusion from side of a half-slab $T^{\perp}$ must be inversely proportional to the distance z_s between the edge and the point-like light source, shortly $1/T^{\perp} = Cz_s$. The proportionality slope C is dependent on the mean free path. This proportionality is quantitatively studied for various porous GaP samples via the transverse effusion microscopy setup. For a subset of samples with relatively longer mean free path (subset1: {J2, J3, D2, B5}), a linear relation between $1/T^{\perp}$ and z_s has been found. This linear behavior can be described by the diffusion theory. For other samples (subset2: {F2, F3, F4, D4}) which have a lower mean free path, a strong deviation from linearity is observed as demonstrated in figure 4.6. The border in scattering strength between the two subsets can be set roughly at $k\ell = 6.5 \pm 1$. Furthermore, the lower the measured mean free path of a sample, the deviation from line starts at lower distances from the source to the edge z_s. To summarize, in a subset of samples for which the mean free

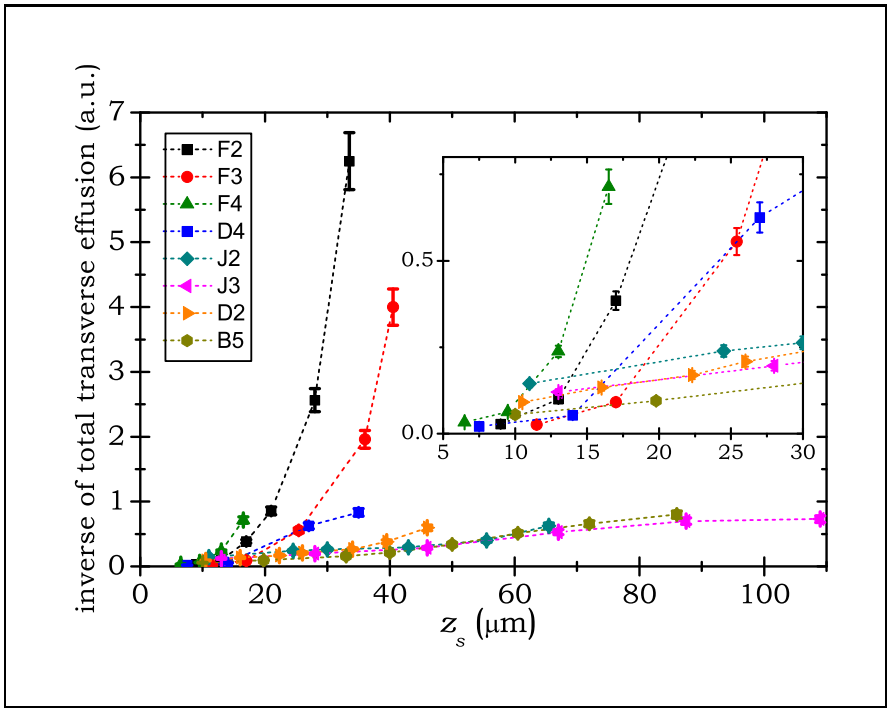

Figure 4.6: *The inverse of total transverse effusion $T^{\perp}$ as measured by the transverse effusion microscopy setup is plotted versus the distance z_s between the focused source and the edge. Deviation from linear diffusive behavior is evident for the subset of samples that possess $k\ell < 6$. The inset is the same data near the origin. Datapoints of each sample are connected with dotted lines as a guide of sight.*

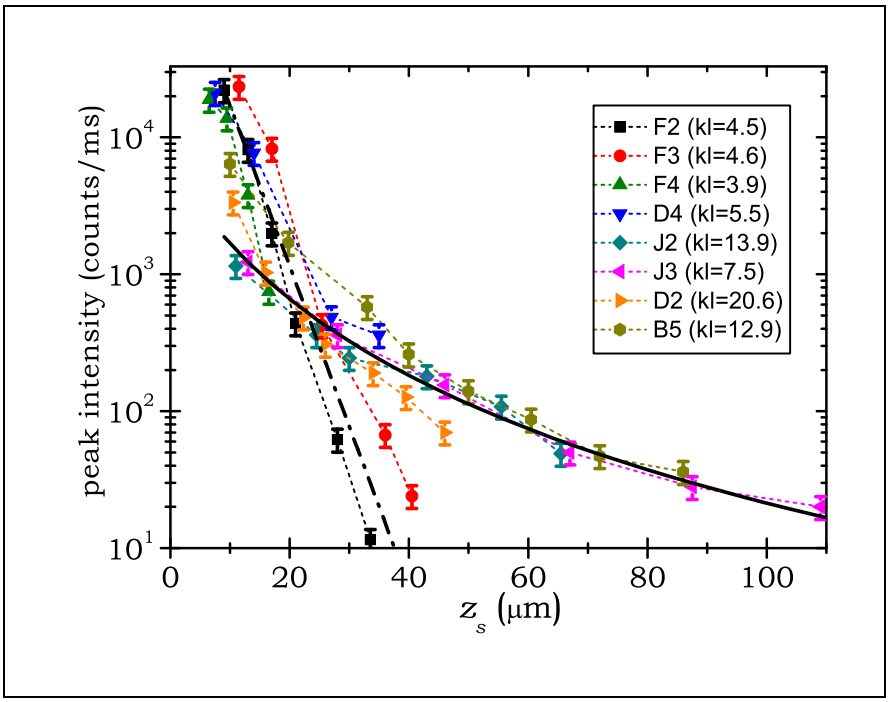

Figure 4.7: *Peak value of transverse effusion function $I^{\perp}_{max}$ versus distance z_s between the illumination spot and the edge of the sample is plotted for several samples. Datapoints of each sample are connected with dotted lines as a guide of sight. The solid line is a fit of cubic decay for sample J3. The thick dash-dot line is a fit of exponential decay for sample F2. The stronger samples show an exponential-decay behavior $\propto \exp(-z_s/L_L)$ rather than cubic decay $\propto z_s^{-3}$ which is the prediction of diffusion theory.*

path is smaller than vacuum wavelength of the probing light, the total transverse effusion decays much faster than the inversely linear behavior predicted by the diffusion theory. This behavior may be thought of as a kind of phase separation happening between these two subsets of GaP samples.

The two subsets of samples show also qualitatively different behavior for the variation of peak value of transverse effusion function $I^{\perp}_{max}$. According to diffusion theory, $I^{\perp}_{max}$ must decrease proportional with z_s^{-3} as the source moves further from the edge. Samples in subset1 show a similar behavior. By contrast, the samples in subset2 deviated strongly from this behavior, see figure 4.7. The distinctive behavior for the samples in subset2 can well be described as an exponential decrease $I^{\perp}_{max} \propto \exp(-z_s/L_l)$ suggestive of localization effects. Here L_l is the localization length. As an example, a result of fitting exponential decay curve to datapoints regarding the sample F2 results in $L_l = 3.8 \pm 0.2$ μm.

The transverse effusion function for the two subsets mentioned above, differ not only in the magnitude but also in the shape of the intensity distribution. To demonstrate this difference I have selected one sample from each subset, namely sample J3 from subset1 and sample F2 from subset2. Here the transverse effusion function is analyzed at a similar source position $z_s = 28 \pm 2$ μm for both of these samples. At this configuration the total transverse effusion and its peak value is one order of magnitude smaller for sample F2 in comparison with sample J3, while the mean free paths just differ by a factor of 2. As seen in figure 4.8(a), the prediction of diffusion theory as stated in equation (2.22) fits very well

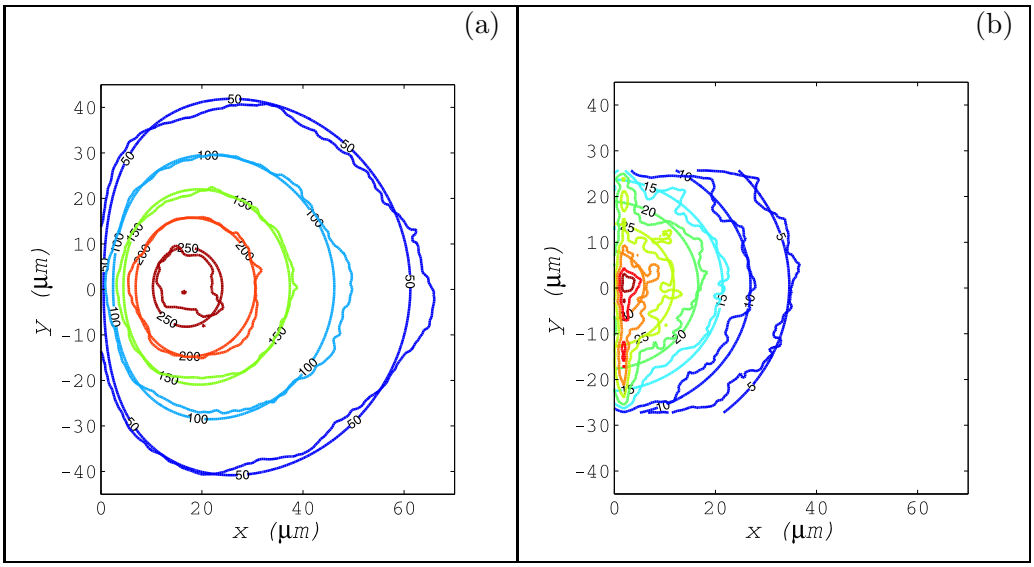

Figure 4.8: (a)*Iso-intensity contours of the transverse effusion function measured on sample J3 (dotted line) is plotted together with a fit (solid line) to the prediction of diffusion theory,equation 2.22. Here z_s and a normalization prefactor are the fitting parameters.* (b)*Iso-intensity contours of athe transverse effusion function measured on sample F2 (dotted line) is plotted over a fit (solid line) to an exponential decay pattern, equation 4.3, which is a characteristic of Anderson localization of light. For both measurements demonstrated here, light is focused at $z_s = 28$ μm from the edge of the sample. From these plots, it is clear that the pattern for J3 does not fit an exponential decay and the pattern for F2 does not fit the prediction of diffusion theory*

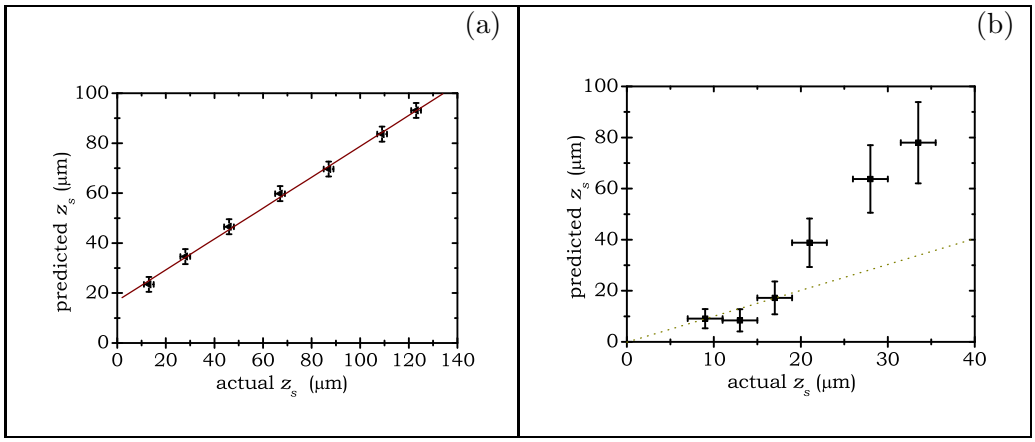

Figure 4.9: (a)*A source position is predicted from fitting the transverse effusion function for sample J3 to the result of diffusion theory. In this plot the prediction is compared with the actual value measured during the experiment. Linear behavior in this graph denotes that diffusion is a proper model. Optical anisotropy can be quantified from the slope of this line.* (b)*The exponential decay function is fitted to the transverse effusion function for sample F2 and the predicted source position is compared with the actual value. The dashed line shows where on the graph the prediction and actual values are identical.*

with the experimental data for sample J3. An adjusting prefactor and the source positions are the two fitting parameters for this graph. The results for sample F2 cannot be fit by equation (2.22) for any reasonable set of fitting parameters. Instead, an exponential decay from the position of the source

$$I^{\perp}(x,y,0) \propto \exp\left(\frac{-\sqrt{(x^2+y^2+z_s^2)}}{L_l}\right) \tag{4.3}$$

fits relatively well to the data using the same L_l extracted from the peak intensity graph of figure 4.7. This fit predicts a value for z_s that can be compared with the actual value to check the correctness of the model. The transverse effusion function for sample J3 does not fit the exponential decay function.

To compare the predictive nature of the two behaviors discussed above, I have fitted equation (2.22) to all the measurements on sample J3 and equation (4.3) to all the measurements on sample F2. In figure 4.9 I have compared the predicted z_s with its actual values. For measurements on sample J3 a linear behavior is observed. The variation from a slope of 1 occurs due to anisotropic diffusion. Using the rescaling discussed in section 2.2.4 in equation (2.22), the ratio between elements of the diagonal diffusion tensor can be found from this slope:

$$\frac{D_{zz}}{D_{xx}} = 2.6 \pm 0.1 \ . \tag{4.4}$$

This result for diffusion tensor agrees remarkably well with the results of transmittance microscopy measurements presented in section 4.2.3. The privilege of measuring anisotropy in half-slab geometry over measuring in the slab geometry is in the extra directions that can be illuminated. If one breaks two times the slab of anisotropic and porous material three orthogonal interfaces of the material are accessible both for illumination and for imaging.

The extracted source positions from fitting exponential decay to measurements on sample F2 exhibits the same trend in agreement with the actual values, as plotted in figure

4.9(b). The prediction is way off the actual value when $z_s > 20$ μm which indicates that a simple exponential decay is a rather premature model for explaining the effusion pattern in this geometry. However the current results are very distinctive, a more rigorous model is required for making a convincing case of observing Anderson localization.

In the next chapter I will discuss second-harmonic generation in porous GaP samples which also shows deviation from prediction of diffusion theory for a few of the inspected samples.

CHAPTER 5

Nonlinear optics with porous GaP

In this chapter, research on optical second-harmonic generation in GaP sponges is presented. The efficiency of conversion is macroscopically measured in several samples with different scattering properties. Good agreement with prediction of diffusion theory is demonstrated for most of the samples. Clear evidence of deviation from diffusive regime is shown for 2 of the 14 samples. The distribution of second-harmonic intensity is shown to be fundamentally different in these two samples from the diffusive case.

5.1 Introduction

Many optical nonlinear processes, in particular frequency doubling, require phase matching to be efficient. Phase mismatch, which is a direct result of dispersion in the nonlinear material, lowers the conversion efficiency, so that in a non-phase-matched case the energy oscillates between the fundamental and second-harmonic waves rather than being transferred in a constant direction. This deficiency is overcome by two main methods. In birefringent and nonlinear material, it is possible to fulfill the phase matching condition by correctly orienting the crystal direction versus the beam. In the other method, called quasi-phase-matching, a periodically polled nonlinearity of the material is arranged such that extra momentum resulted from the phase-mismatch can be transferred to the crystal. In both methods, the total conversion yield increases quadratically with the length of light path inside the medium.

Random quasi-phase-matchingis recently shown to be an effective way of enhancing conversion efficiency in isotropic nonlinear dielectrics[29]. By randomly reorienting the crystal direction in the beam path, i.e. using a powder, a conversion yield that is linearly increasing with sample thickness is achieved. The same conversion mechanism and increase in the total nonlinear conversion yield of the scattering media was reported by Tiginyanu *et al* for porous GaP[42]. Mel'nikov and coworkers have studied anodically-etched GaP sponges and reported unexpectedly large variation in the efficiency of second-harmonic

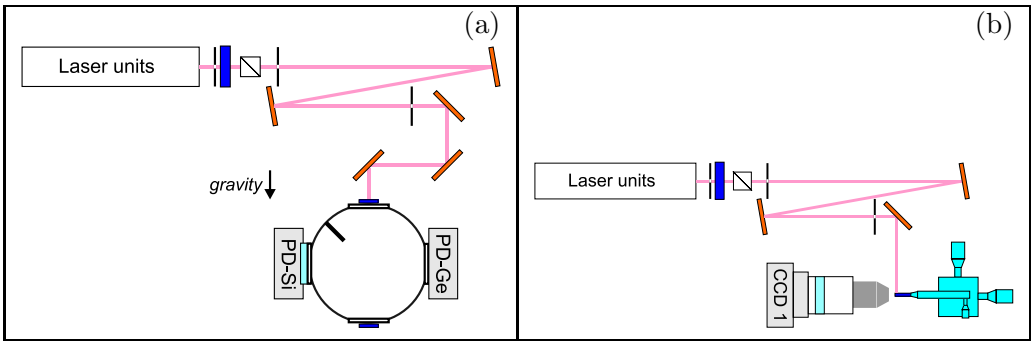

Figure 5.1: *Schematic view of experimental setups for second-harmonic measurements.* (a) *The porous-GaP slab is illuminated with a parallel beam of 120 femtosecond infrared pulses. The integrating sphere collects the fundamental and second-harmonic light scattered at all angles on one side of the sample. The sample lies on the sphere for transmission measurements and beneath the sphere for reflection measurements. A Silicon photodetector behind a cold glass filter measures the second-harmonic signal in the visible range. Meanwhile a Germanium photodetector measures the infrared fundamental light.* (b) *The transverse effusion microscopy setup images the second-harmonic signal that is radiated from the narrow side of a broken GaP slab while it is illuminated by a parallel beam of infrared pulses.*

generation as the fundamental light wavelength is changed from 1.0 to 1.6 μm[43, 44]. No convincing explanation has yet been proposed for this anomalous effect. The only rigorous theoretical study of optical second-harmonic generation in scattering media considers only the case of weakly scattering material[26].

The second-harmonic signal generated in a random material can be a very informative probe of light distribution inside the scattering medium. Second harmonic signal has been used to study angular, spatial and temporal correlations inside scattering media[30, 45, 46]. As the second-harmonic signal is quadratically dependent on the fundamental light power, it can be a very sensitive probe of local field enhancement, for example in the case of Anderson localization of light. A rigorous formalism of optical nonlinear behavior in the Anderson localization regime is still lacking.

In what follows, I describe a setup for measuring total nonlinear yield of opaque slabs. This yield has been measured for various porous GaP samples. The diffusive behavior is tested using the measurements on far-field distribution of light at either side of the slab and near-field measurement of second-harmonic effusion function at the narrow side of a broken slab. Two samples deviate from diffusive regime in both experiments.

5.2 Yield measurements

Second-harmonic conversion yield at a fundamental wavelength of 1.2 to 1.6 μm is measured for various samples in order to check the diffusion model for this nonlinear process in an opaque object. Far-field intensity is integrated over 2π spherical angle at each side of the slab. Radiation toward the side that includes the incident beam is called the backward radiation. Radiation in the opposite direction is called the forward radiation.

5.2.1 Integrating sphere setup

The second-harmonic light that is generated in an opaque objects propagates at all directions. The angular distribution is symmetric for optically thick samples. Therefore measuring in a selected angle can be a good representative of the total yield. To avoid speckle and directional effects it is preferable to collect light at the maximum angular spread. Thus an integrating sphere is used for these measurements.

The setup that is sketched in figure 5.1(a) is used for measuring the total second-harmonic light propagating in the forward and backward direction from a porous-GaP slab. The conversion efficiency in porous GaP is higher than crystalline bulk GaP, but it is yet much lower than a commercial second-harmonic crystal such as KDP. For a second-harmonic signal to be detectable for normal silicon detectors, an incident intensity of few GW/cm^2 is needed. A long pulse at this power will evaporate GaP, therefore pulses shorter than nanoseconds with low repetition rates are needed. Here, the light source is a traveling-wave collinear optical parametric amplifier of super-fluorescence(TOPAS - Light Conversion) pumped with a femtosecond laser (Hurricane - Spectra Physics) at 800 nm. The TOPAS wavelength can be tuned continuously from 1150 to 2200 nm. The output beam contains three different frequencies. The desired beam at infrared frequencies is selected using a Glan-Taylor prism and a low-pass filter (RG850 - Thorlabs).

Several gold mirrors guide the beam vertically into the entrance of a TiO_2 coated integrating sphere. The sample can be laid down at the entrance for transmission measurements or placed beneath the sphere for reflection measurements. Two photodiodes are positioned at the two exit holes of the integrating sphere. an amplified Silicon detector (PDA55a - Thorlabs) D2 connected to an oscilloscope (DL9040L - Yokogawa) measures the second-harmonic signal after the fundamental infrared light is filtered by cold glass filter (KG5). Simultaneously, a Germanium detector (DET10A - Thorlabs) D1 connected to another channel of the same oscilloscope, measures the scattered fundamental light. The D1 signal is used for measuring the optical thickness of each sample for the incident wavelength.

Before each measurement, the incident power is checked by a pyroelectric head and a power meter (Ophir). For each sample, first the fundamental and second harmonic light in the forward direction is measured in a wavelength range of 1.2 to 1.6 μm while the beam is incident on the substrate of the sample. Then the sample is flipped and the same measurements are repeated. After these measurements, the sample is placed beneath the sphere while the beam is incident on the etched side. The fundamental and second-harmonic light propagating in the backward direction is then measured in the same wavelength range as previous.

The transmittance of filters and responsivities and linearity of detectors are carefully taken into account before extracting the second-harmonic yield.

5.2.2 Dependence on incident power

At a wavelength of 1250 nm, the dependence of second-harmonic signal on incident power is measured for several samples in the forward direction. In a second-order nonlinear process the second-harmonic intensity is proportional to the square of incident power. A consistent power-law dependence between incident and second-harmonic powers is evident for all the samples as plotted in figure 5.2. The result of fitting a power law $P^{(2)} \propto P_0^{\alpha}$ is $\alpha = 1.81 \pm 0.03$ rather than 2.0. This deviation may be a sign of local heating or nonlinear absorption inside the porous-GaP but this effect will not be further pursued in this thesis.

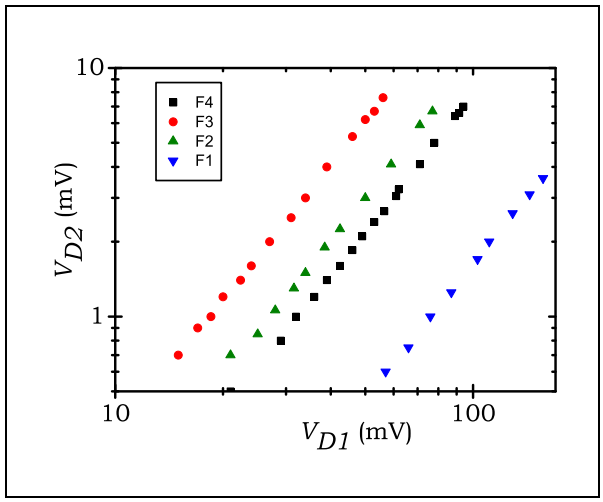

Figure 5.2: *The signal detected by silicon detector V_{D2} is plotted versus the signal detected by Germanium detector V_{D1} in logarithmic scales. The second-harmonic power is proportional to V_{D2} and increases almost quadratically with the incident power which is proportional to V_{D2}.*

5.3 Far-field distribution

It is derived in section 2.6.3 that according to the photon diffusion theory, the efficiency of nonlinear conversion shows up in total second-harmonic light propagating out in the backward or the forward direction relative to the incident beam, $R^{(2)}$ and $T^{(2)}$. This dependency cancels out when taking the ratio of these two quantities. Thus the ratio depends only on the scattering properties of the sample. Therefore, this backward-forward ratio $\eta = R^{(2)}/T^{(2)}$ is a proper quantity for comparing scattering properties of different samples while they have different nonlinear conversion yields.

5.3.1 Backward-forward ratio

By using the integrating sphere setup described in section 5.2.1 the backward-forward ratio η is measured for various GaP sponge samples. Light is incident on the etched side of the sample for measurements of both $T^{(2)}$ and $R^{(2)}$. The incomplete transmittance of GaP substrate thus should be considered in the measurements of $T^{(2)}$. Based on Fresnel equations, the angular averaged transmittance of the GaP substrate has been calculated to be 0.36. Considering this correction, η has been plotted versus the optical thickness of the samples at the fundamental wavelength in figure 5.3, where the optical thickness is measured simultaneously using the Ge detector in the setup.

The prediction of non-stationary diffusion equation derived in section 2.6.3 is also plotted for comparison. The pulse length is taken equal to the sample thickness for this calculation. Complete consideration of the effect of substrate and reflectivities at the interfaces between the air, the etched slab, and the substrate is rather cumbersome. These effects may change η by a maximum factor of two. It should also be noted that the backward and forward radiation could not be measured simultaneously. Considering these uncertainties, the agreement between measurement and theory is qualitatively good for most of the samples. For these samples, however, the measured ratio η systematically deviate from the theory curve; it is lower that what is expected. This deviation is within the limits of uncertainties and

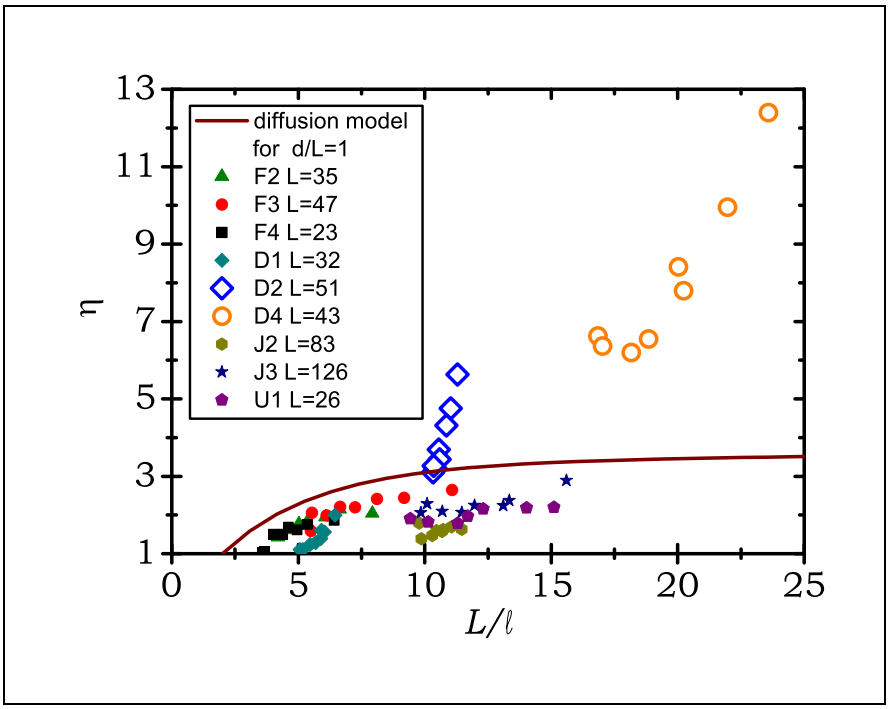

Figure 5.3: *The ratio between total second-harmonic light propagating out in the backward or the forward direction η is plotted versus the optical thickness for various wavelength and samples. The non-stationary diffusion prediction from section 2.6.3 is plotted as a solid line. Two of the samples, D2 and D4, show a large enhancement, inconsistent with the diffusion theory.*

can also be related to the inefficiency of the integrating sphere, which also shows up in the sum of the linear transmission and reflection.

Meanwhile, two of the samples are undoubtedly exceptional. The ratio η for samples D2 and D4 is much higher than the diffusion-theory prediction. This deviation cannot be described by normal interfacial corrections to the diffusion theory. In the following this phenomenon is further discussed.

5.3.2 Deviation from diffusion theory prediction

Samples D2 and D4 deviate in their behavior from diffusion theory. In the illumination wavelength range used for these experiments, these two samples have the smallest mean free path of all the samples, $\ell \sim 2$ μm. Sample U1 is another sample that has similar mean free path but doesn't show enhancement. It may be relevant to mention that the thickness of U1 is almost half that of D2 and D4. Different hypotheses are put forward for the enhancement of backward-forward ratio η for two samples D2 and D4.

One hypothesis is that nonlinear yield at the surface is much higher that in the bulk of the porous material and dominates the ratio. It is known that second-order nonlinear processes can be much more efficient at the interfaces because of the symmetry breaking. The variation between samples is then due to difference in their surface properties, which happens due to different surface treatment procedures. This hypothesis was ruled out by measuring the distribution of second-harmonic inside the samples by microscopic imaging of second-harmonic transverse effusion function at the section of the sample. There it is shown that the peak of second-harmonic intensity occurs well inside the slab and that much

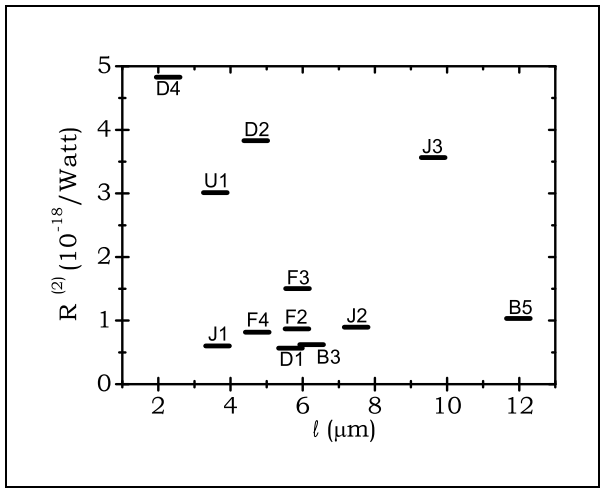

Figure 5.4: *The absolute yield of second-harmonic intensity propagating in the backward direction for fundamental wavelength of* $\lambda_0 = 1300$ nm.

more light is produced in the bulk than the surface. The experiment is described in more detail in section 5.4.1.

The second hypothesis questions the assumptions of the diffusion theory regarding the nonlinear conversion mechanism. In deriving the diffusion result, it was assumed that the source distribution of second-harmonic photons is proportional to square of diffusive photon distribution of the fundamental wavelength. It is not clear if any experiment has proven this assumption in strongly scattering material. If on average, conversion efficiency for fundamental diffusive photons is much less than for the coherent incident beam, this assumption goes wrong. In this case, the conversion happens only in the skin layer before the first mean free path. Assuming the source of second harmonic diffusive photons is concentrated in the skin layer, the solution to diffusion equation for second-harmonic photons gives a backward-forward ratio η that is linearly proportional to the optical thickness at the fundamental wavelength, (as in the case of the fundamental). This result is not valid as presented in figure 5.3. Besides, the transverse effusion pattern can also rule out this hypothesis as the source of second-harmonic photons is well distributed inside the slab. If the conversion happens only before the first scattering event, it is expected that samples with lower mean free path will show smaller conversion yield which is not at all the case according to the plot in figure 5.4.

Another hypothesis is related to the nonlinear absorption at the triple frequency, which is inside the electronic bandgap of GaP, due to nondegenerate two-photon mixing. In principle this effect must be relatively very weak because it is a third order process modulating a second order process, for which the yield is already very low ($\sim 10^{-9}$). Even if this absorption was a dominant effect, the dependence of second-harmonic power on fundamental power should have deviated more from quadratic behavior, near the higher values of the incident power, see figure 5.2.

All the above hypotheses, question the predictions of diffusion theory. If such a wrong prediction is made, it should be invalid for all of the samples. None of these hypotheses can describe the evident difference in behavior of the samples D2 and D4 with the rest of the samples.

In the last hypothesis I propose that the distribution of fundamental light intensity is

intrinsically different from the diffusion theory prediction. Unlike the diffusive regime for which this intensity drops linearly inside the sample, in the Anderson localization regime, the intensity must drop exponentially. The resonant interference in this regime also adds to the total yield due to accumulation of energy at the localized region. There is yet no theory available for optical nonlinear processes in the Anderson localization regime, therefore this hypothesis cannot be indeed proven. Nevertheless, it may be the best available description for the enhancement that is observed in the two samples.

5.4 Internal distribution

In order to investigate the second-harmonic energy distribution inside a porous GaP sponge, the transverse effusion function is measured. This measurement may help in retrieving the distribution of the second-harmonic source. The prediction of diffusion model for an infinite slab is presented in section 2.6.3. The effusion function at the side of half-slab is in principle different from the distribution inside the slab. This effusion function has been calculated numerically assuming diffusive conditions. At it turns out, the second-harmonic effusion pattern roughly approximates the bulk second-harmonic energy distribution. Therefore one can get an immediate qualitative sense of the second-harmonic energy distribution from the nonlinear transverse effusion function.

5.4.1 Transverse effusion at second-harmonic frequency

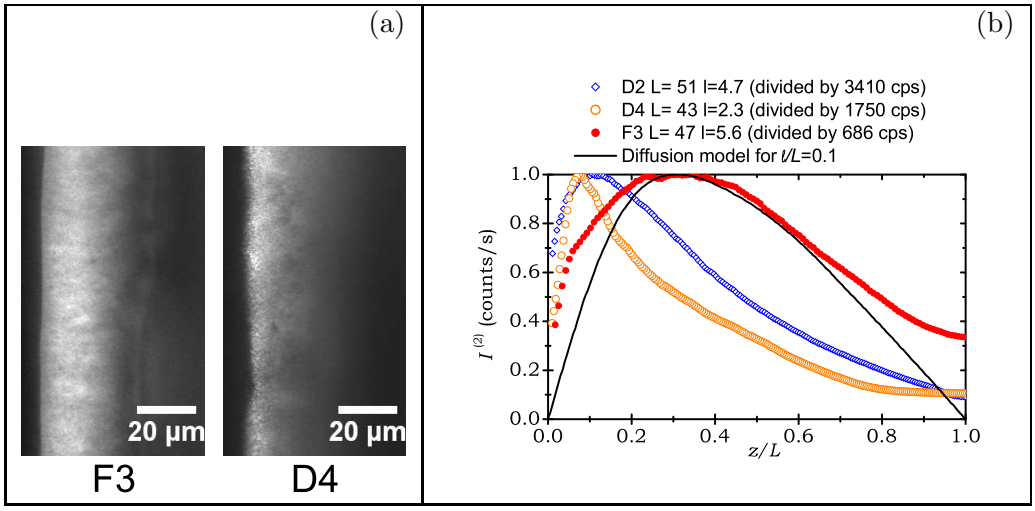

Figure 5.5: (a) *Micrograph of second-harmonic effusion from section of the porous-GaP slab while it is illuminated with a parallel beam of infrared pulses. Brighter regions indicate higher effusion of second-harmonic light.* (b) *The average of transverse effusion, with its peak normalized to one, is plotted versus the position inside the sample (symbols) and is compared with the prediction of non-stationary diffusion model (solid line) presented in section 2.6.3 for a specific optical thickness.*

The transverse effusion microscopy setup is used to capture the second-harmonic effusion pattern. This setup is schematically drawn in figure 5.1(b) and resembles the transverse effusion microscopy setup described in section 4.3.1. The incident beam in this setup is a gaussian infrared beam of $\sim$ 3 mm in diameter with its center positioned at the edge of

the sample. There is a cold glass filter in front of the CCD camera so that only the visible second-harmonic light is captured. Actually, the CCD is not sensitive to the infrared at frequencies used in this experiment, but since the intensity of infrared light is much higher than the visible and it may add to the noise and background of the measurements via the two photon absorption at the detector.

During the experiment on each sample, three images are taken. The first image is an ambient-light micrograph from the section. The second image is the second harmonic transverse effusion pattern (see figure 5.5(a) as an example.) The third image captures the linear transverse effusion pattern by tuning the incident beam at half the wavelength of its value in previous image, without changing the position of the beam on the sample.

5.4.2 Special behavior in outliers

Transverse effusion function at the second-harmonic frequency were recorded for three samples F3, D2 and D4. The backward-forward ratio η in sample F3 shows a general agreement with the non-stationary diffusion model. It has been selected because sample F3 possesses one of the lowest mean free paths in the visible range. The other two samples, D2 and D4 show enhanced values of η which contradicts the diffusion model. The results are presented in figure 5.5(b) as the normalized intensity distribution versus the normalized depth of penetration inside the sample. This images leave no doubt that nonlinear conversion is indeed happening inside the slab and that the surface effects are not a relevant factor for the present experimental quantities. Thus, the first and second hypotheses introduced in the previous section are ruled out.

According to the diffusion model, all the experimental distributions for these 3 samples must be almost the same. The variation in the theoretical curve caused by changing the optical thickness by a factor of two is not noticeable in comparison to the variations in the measurements. The prediction of diffusion model for second-harmonic energy distribution inside an slab is thus plotted only for a specific optical thickness as a reference. The nonlinear transverse effusion function of sample F3 resembles the model. The deviation near the two sides may be explained by the finite reflectivity of these boundaries (the extrapolation length) that are neglected in the calculations of chapter 2. However boundary effects cannot describe the obscured deviation of samples D2 and D4.

Qualitatively, it may be suggested that the negative curvature in the effusion curves of D2 and D4 denote a narrowly distributed conversion spread in the bulk of the sample. The narrow distribution of diffusive photons at fundamental frequency may be a result of Anderson localization, but this claim cannot be explicitly proven until a theory for nonlinear processes in the Anderson localization regime is developed.

It is possible to measure the total transverse effusion at infrared wavelength, and directly investigate presence of Anderson localization in an experiment similar to what is introduced in section 4.3. I propose this experiment as a further step in investigation of non-diffusive behavior of the specified samples.

CHAPTER 6

Conclusion

In this chapter an overview of the results reported in the previous chapters is presented. The major achievements are highlighted and recommendations for further research are given.

6.1 Summary of experiments

The experiments described in the previous chapters were optimized for very strongly scattering samples near the threshold of transition to the Anderson localization regime. Both continuous light sources and ultrashort pulses were used. Thus, both stationary and non-stationary diffusion theories were needed for comparison. The nonlinear-optical properties of these sample were also investigated.

A group of porous-GaP samples used in other research projects was selected. These samples were analyzed together with three new samples of the same type, specifically fabricated for this project. All these samples were experimentally characterized in a similar procedure by analysis of SEM micrographs, total transmission, and enhanced backscattering. The sample specifications are listed in 3.3.2.

The linear-optical experiments in the stationary-regime were mainly discussed in chapter 4. Two new experimental procedures were presented. In transmittance pattern microscopy, introduced in section 4.2.1, the near-field intensity distribution on the surface of an opaque slab, namely the effusion function, was measured while light was focused on the opposite side of the slab. If the sample is isotropically scattering, the overall shape of the transmittance pattern is indicative of the sample thickness, independent of its mean free path. Thus, this method can be used for measuring the thickness of an isotropic opaque slab, without breaking it for looking at its cross section. For sample that are optically anisotropic, given the sample thickness, this method can be indicative of anisotropy along the direction perpendicular to the slab.

If the cross section of an opaque slab is accessible, the radiation of light from a side orthogonal to the illumination side can be measured. This near-field intensity distribution

on the side is referred to as transverse effusion function. Measuring in this configuration has a main advantage over the measurement on a slab. Here, the distance between light source and measurement interface can be varied in a single sample. This variation is essential for several experiments including those that investigate the onset of Anderson localization. Previously, for such an experiment several samples of different thicknesses were needed in which thus sample-to-sample variations added to the experimental error.

The transverse effusion microscopy can also be useful for determination of optical anisotropy. By conducting this experiment, a subset of samples that showed non-diffusive behavior were discovered.

The nonlinear-optical experiments were mainly discussed in chapter 5. The ratio of total second-harmonic radiation in the backward and forward direction is known to be independent of the nonlinear conversion efficiency of a scattering slab. Thus, this quantity was measured for several samples at the fundamental wavelength range of 1.2 to 1.6 μm. A qualitative agreement with the diffusion theory was observe for most of the samples. Clear deviation from this behavior was observed for 2 samples out of 14.

To further investigate the nonlinear mechanism, transverse effusion pattern of the second-harmonic light was measured. This experiment confirmed the assumption that nonlinear conversion is distributed in the bulk of the sample and the surface effects are not of primary importance.

6.2 To diffuse or not to diffuse

The diffusion theory is very successful in explaining most of the effects that are observed in strongly scattering media. In the transition to the Anderson localization regime interference effects become so important that the diffusion theory will break down. Observation of Anderson localization of light is a holy grail for Optics researchers. Different experimental configurations have previously been proposed to check the limits of validity of the diffusion model for scattering media. Many of them have confirmed the agreement for weakly scattering materials and a few cases of deviation have been reported for the limit of strong scattering.

In the new experiments that were introduced in the previous chapters, it has been shown that diffusion theory can model the details of light distribution inside and around several strongly scattering samples. However, exceptional behavior was observed for some samples which may indicate to the breakdown of diffusion theory.

6.2.1 Confirmation cases

Although I have used a very simplified version of diffusion theory for deriving the theory presented in chapter 2, the measurements results were in good agreement with the theoretical predictions for most of the experiments, in particular the transmittance patterns (section 4.2) and the transverse effusion patterns (section 4.3.)

For the second-harmonic generation measurements, the exact conversion mechanism and its dependence on the scattering properties of the sample remains an open question. The yield factor cancels out in the backward-forward ratio η (see section 2.6.3 for the theory and section 5.2 for the experiment.) Although a qualitative agreement between the theory and the experiment was indicated, more details of the interfacial effects should be determined in order to experimentally confirm the theory.

6.2.2 Violation cases

The transverse effusion microscopy experiments offered the opportunity to check the inverse-linearity of transmittance with the effective thickness in a single sample. Using this setup clear deviation from diffusion theory was demonstrated in section 4.3.2 for a subset of samples. The distinctive effusion patterns for these samples confirms the observation.

In measuring the backward-forward ratio η for second-harmonic radiation, strong enhancement was observed for 2 out of 14 samples. It was shown that this enhancement is much too large to be explained by interfacial effects. Interestingly, samples that show deviation in the stationary experiments are not the same as those that stand out in nonlinear measurements. This difference is perhaps due to the variable scattering strength of the samples at the probing frequency range.

6.3 Follow up research

Many of the experiments that were presented in the previous chapters were exploratory experiments. Many details can still be investigated. In some cases, more samples should be analyzed to produce firm conclusions.

In the stationary measurements, using a broadband source of light will be helpful in averaging the surface speckle pattern and will increase the precision of the measurements. Repeating these experiments at various light frequencies will provide extra information about the samples, specially for those that deviate from diffusive behavior.

The half-slab geometry has shown to be very helpful in investigating the transport properties of an individual samples. Time-resolved experiments on this type of samples with the illumination beam orthogonal to the detection direction may be very informative about time of flight and resonant effects.

All the nonlinear experiments may be repeated with a focused source. The spread of nonlinear processes in the scattering material can be further investigated in a half-slab, which provides more information about second-harmonic source distribution inside random media. In a narrow-band-width experiment, analysis of the speckle pattern of the second-harmonic light will also help to explain the nonlinear conversion mechanism in random media.

Bibliography

[1] A. Yodh and B. Chance, *Spectroscopy and imaging with diffusing light*, Physics Today **48**, 3440 (1995). — p.16.

[2] G. Bergmann, *Physical interpretation of weak localization: A time-of-flight experiment with conduction electrons* , Phys. Rev. B **28**, 2914 (1983). — p.16.

[3] M.P. van Albada and A. Lagendijk, *Observation of weak localization of light in a random medium*, Phys. Rev. Lett. **55**, 2692 (1985). — p.16 and 37.

[4] P.E. Wolf and G. Maret, *Weak localization and coherent backscattering of photons in disordered media*, Phys. Rev. Lett. **55**, 2696 (1985). — p.16.

[5] P.W. Anderson, *Absence of diffusion in certain random lattices*, Phys. Rev. **109**, 1492 (1958). — p.16.

[6] T.R. Kirkpatrick, *Localization of acoustic waves*, Phys. Rev. B **31**, 5746 (1985). — p.16.

[7] R. Bruinsma and S.N. Coppersmith, *Anderson localization and breakdown of hydrodynamics in random ferromagnets*, Phys. Rev. B **33**, 6541 (1983). — p.16.

[8] L. Sanchez-Palencia, D. Clément, P. Lugan, P. Bouyer, G.V. Shlyapnikov, and A. Aspect *Anderson localization of expanding Bose-Einstein condensates in random potentials*, Phys. Rev. Lett. **98**, 210401 (2007). — p.16.

[9] T. Paul, P. Schlagheck, P. Leboeuf, and N. Pavloff, *Superfluidity versus Anderson localization in a dilute bose gas*, Phys. Rev. Lett. **98**, 210602 (2007). — p.16.

[10] D.S. Wiersma, P. Bartolini, A. Lagendijk and R. Righini, *Localization of light in a disordered medium*, Nature **390**, 671 (1997). — p.17, 27, and 45.

[11] H. De Raedt, A. Lagendijk, and P. de Vries, *Transverse localization of light*, Phys. Rev. Lett. **62**, 47 (1989). — p.17.

[12] T. Schwartz, G. Bartal, S. Fishman, M. Segev, *Transport and Anderson localization in disordered two-dimensional photonic lattices*, Nature **446**, 52 (2007). — p.17.

[13] P. Lodahl, A.P. Mosk, and A. Lagendijk, *Spatial quantum correlations in multiple scattered light*, Phys. Rev. Lett. **95**, 173901 (2005). — p.20.

[14] I.M. Vellekoop, P. Lodahl, and A. Lagendijk, *Determination of the diffusion constant using phase-sensitive measrements*, Phys. Rev. E **71**, 056604 (2005). — p.20.

[15] M.C.W. van Rossum and Th.M. Nieuwenhuizen, *Multiple scattering of classical waves: microscopy, mesoscopy, and diffusion*, Rev. Mod. Phys. **71**, 313 (1999). — p.22 and 24.

[16] B.A. van Tiggelen, A. Lagendijk, M.P. van Albada, and A. Tip, *Speed of light in*

random media, Phys. Rev. B **45**, 12233 (1992). — p.22.

[17] B.A. van Tiggelen and Eugene Kogan, *Analogies between light and electrons: Density of states and Friedel's identity*, Phys. Rev. A **49**, 708 (1994). — p.22.

[18] P.W. Anderson, E. Abrahams, and T.V. Ramakrishnan, *Possible explanation on nonlinear conductivity in thin-film metal wires*, Phys. Rev. Lett. **43**, 718 (1979). — p.22.

[19] P.N. den Outer, Th.M. Nieuwenhuizen, and A. Lagendijk, *Location of objects in multiple-scattering media*, J. Opt. Soc. Am. A **10**, 1209 (1993). — p.23.

[20] A. Lagendijk, R. Vreeker, and P. de Vries *Influence of internal reflection on diffusive transport in strongly scattering media*, Phys. Lett. A **136**, 81 (1989). — p.24 and 25.

[21] J.X. Zhu, D.J. Pine, and D.A. Weitz, *Internal reflection of diffusive light in random media* , Phys. Rev. A **44**, 3948 (1991). — p.24.

[22] R. Aronson, *Boundary conditions for diffusion of light*, J. Opt. Soc. Am. A **12**, 2532 (1995). — p.24.

[23] S. Fantini, M.A. Franceschini, and E, Gratton, *Effective source term in the diffusion equation for photon transport in turbid media*, Applied Optics **36**, 156 (1997). — p.24.

[24] P.M. Johnson, B.P.J. Bret, J.G. Rivas, J.J. Kelly, and A. Lagendijk, *Anisotropic diffusion of light in a strongly scattering material*, Phys. Rev. Lett. **89**, 243901 (2002). — p.27 and 45.

[25] P.M. Johnson, A. Imhof, B.P.J. Bret, J.G. Rivas, and A. Lagendijk, *Time-resolved pulse propagation in a strongly scattering material*, Phys. Rev. E **68**, 016604 (2003). — p.27.

[26] V.E Kravtsov, V.M. Agranovich, and K.I. Grigorishin, *Theory of second harmonic generation in strongly scattering media*, Phys. Rev. B **44**, 5931 (1991). — p.30 and 54.

[27] A. Heiderich, R. Maynard, B.A. van Tiggelen, *Coherent backscattering in nonlinear media*, Optics Communications **115**, 392 (1995). — p.30.

[28] E.V. Makeev, S.E. Skipetrov, *Second-harmonic generation in suspensions of spherical particles*, Optics Communications **224**, 139 (2003). — p.30 and 31.

[29] M. Baudrier-Raybaut, R. Haïdar, Ph. Kupecek, Ph. Lemasson, and E. Rosencher, *Random quasi-phase-matching in bulk polycrystalline isotropic nonlinear materials*, Nature **432**, 374 (2004). — p.30 and 53.

[30] J.F. de Boer, A. Lagendijk, R. Sprik, and S. Feng *Transmission and reflection correlations of second-harmonic waves in nonlinear random media*, Phys. Rev. Lett. **71**, 3947 (1993). — p.30, 32, and 54.

[31] B.H. Erné, D. Vanmaekelbergh, J.J. Kelly, *Morphology and strongly enhanced photoresponse of GaP electrodes made porous by anodic etching*, J. Electrochem. Soc. **143**, 305 (1996). — p.35.

[32] F.J.P. Schuurmans, D. Vanmaekelbergh, J. van de Lagemaat, and A. Lagendijk, *Strongly photonic macroporous GaP networks*, Science **284**, 141 (1999). — p.35 and 45.

[33] J.G. Rivas, *Light in strongly scattering semiconductores - diffuse transport and Anderson localization*, PhD Thesis, Universiteit van Amsterdam, Amsterdam (2002). — p.35.

[34] K.L. van der Molen, R.W. Tjerkstra, A.P. Mosk, and A. Lagendijk, *Spatial extent of random laser modes*, Phys. Rev. Lett. **98**, 143901 (2007). — p.35.

[35] F.J.P. Schuurmans, M.Megens, D. Vanmaekelbergh, and A.Lagendijk, *Light scattering*

near the localization transition in macroporous GaP networks, Phys. Rev. Lett. **83**, 2183 (1999). — p.35.

[36] B.P.J. Bret, *Multiple light scattering in porous gallium phosphide*, PhD Thesis, Universiteit Twente, Enschede (2005). — p.35.

[37] R.W. Tjerkstra, *Electrochemical Formation of Porous GaP in Aqueous HNO_3*, Electrochem. Solid-State Lett. **9**, C81 (2006). — p.35.

[38] D.E. Aspnes, A.A. Studna, *Dielectric functions and optical parameters of Si, Ge, GaP, GaAs, GaSb, InP, InAs, and InSb from 1.5 to 6.0 eV*, Phys. Rev. B **27**, 985 (1983). — p.37.

[39] S Adachi, *Optical dispersion relations for GaP, GaAs, GaSb, InP, InAs, InSb, $Al_xGa_{1-x}As$, and $In_{1-x}Ga_xAs_yP_{1-y}$* , J. Appl. Phys. **66**, 6030 (1989). — p.37.

[40] M. Störzer, P. Gross, C.M. Aegerter, and G. Maret, *Observation of the critical regime near Anderson localization of light*, Phys. Rev. Lett. **96**, 063904 (2006). — p.45.

[41] J. Taniguchi, H. Murata, and Y. Okamura, *Light diffusion model for determination of optical properties of rectangular parallelepiped highly scattering media*, Applied Optics **46**, 2649 (2007). — p.45.

[42] I.M. Tiginyanua, I.V. Kravetsky, J. Monecke, W. Cordts, G. Marowsky, and H.L. Hartnagel, *Semiconductor sieves as nonlinear optical materials*, Appl. Phys. Lett. **77**, 2415 (2000). — p.53.

[43] V.A. Melnikov, L.A. Golovan, S.O. Konorov, D.A. Muzychenko, A.B. fedotov, A.M. Zheltikov, V.Yu. Timoshenko, and P.K. Kashkarov, *Second-harmonic generation in strongly scattering porous gallium phosphide*, Appl. Phys. B **79**, 225 (2004). — p.54.

[44] V.A. Melnikov, L.A. Golovan, K.P. Bestemyanov, S.V. Zabotnov, V.M. Gordienko, V.Yu. Timoshenko, A.M. Zheltikov, and P.K. Kashkarov, *Disorder-correlated enhancement of second-harmonic generation in strongly photonic porous gallium phosphide*, Appl. Phys. B **81**, 353 (2005). — p.54.

[45] T. Ito and M. Tomita, *Speckle correlation measurement in a disordered medium observed through second-harmonics generation* , Phys. Rev. E **69**, 036610 (2004). — p.54.

[46] M. Tomita, *Coherence coupling effect in a space- and time-resolved, nonlinear-correlation measurement in a multiple-scattering medium*, J. Opt. Soc. Am. B **22**, 537 (2005). — p.54.

APPENDIX A

Compact setup for recording enhanced backscattering

Enhanced backscattering(EBS) is a result of the most robust interference effects that survives multiple scattering. When a strongly scattering object is illuminated with coherent light the constructive interference of time-reversed paths, on average, leads to a net increase of light transport in the backward direction. The general shape of EBS versus measurement angle resembles a cone with a sharp peak at an angle of zero relative to the incidence direction[1]. The amount of enhancement at the peak of the cone is twice the background scattered intensity. The function describing the EBS cone for an isotropic media is

$$I(\alpha) = A \times \frac{2(1+\tau-\frac{1}{1+\cos\alpha})\cos\alpha + (E_f-1)[k\ell\,|\sin\alpha| + \frac{1+\cos\alpha}{2}(1+\frac{\tau k\ell\,|\sin\alpha|-1}{\tau k\ell\,|\sin\alpha|+1})]}{k\ell\,|\sin\alpha|(1+2\tau)(\frac{1+\cos\alpha}{2})[(k\ell)^2(1-\cos\alpha)^2+(k\ell\,|\sin\alpha| + \frac{1+cos\alpha}{2})^2]}, \quad \text{(A.1)}$$

where $I(\alpha)$ is the intensity propagating at an angle α with the incidence direction, k is the wave number and ℓ is the mean free path. The enhancement factor E_f denotes the effect of single scattering events which do not contribute to EBS. The prefactor A is for normalization of the measurements and τ denotes the effect of finite reflection at the interfaces. For index-matched interfaces $\tau = \frac{2}{3}$.

The schematic setup for measuring enhanced backscattering is illustrated in figure A.1. The setup is build on an optical bread-board. A HeNe laser is always included in the setup. Using a flipping mirror, other sources can also be fed to the setup for measurements at different light frequencies. The laser beam is expanded by a set of lenses and a and then polarized. A glass beam-splitter, which is anti-reflection coated on its back, reflects light on the sample. The scattered light from the sample is gathered using a focus-matched system of 2-inch BK7 lenses. A CCD-camera (Mightex) equipped with a photography lens (Pentax $f50\,\phi50$) and a polymer polaroid records the signal.

The angle corresponding to each pixel on the CCD is calibrated by placing a grating in the position of the sample. The grating generates a diffraction pattern of lines with an

[1] see B.P.J. Bret, *Multiple light scattering in porous gallium phosphide*, PhD Thesis, Universiteit Twente, Enschede (2005).

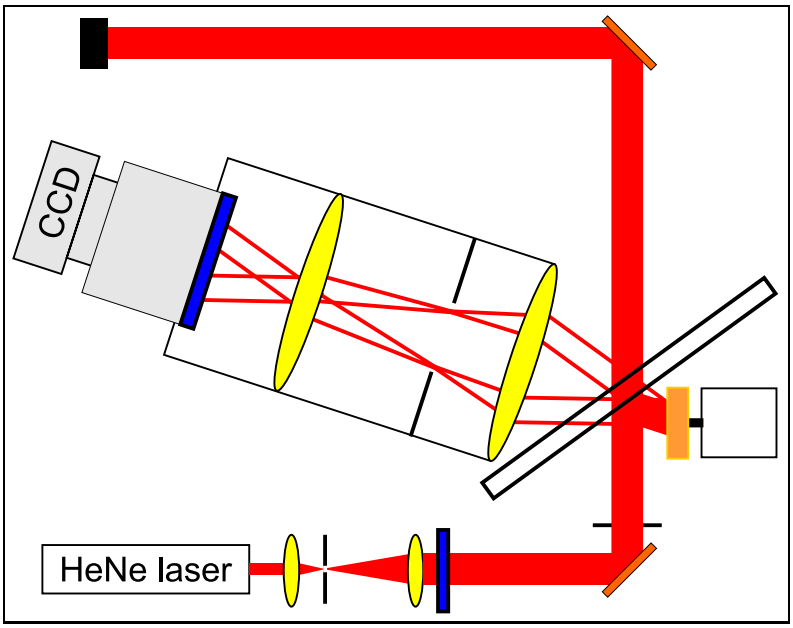

Figure A.1: *Schematic view of experimental setup for measuring enhanced backscattering. The incident beam is expanded and polarized by a set of lenses and a linear polarizer. The reflection of the beam from a beam-splitter illuminates the sample mounted on a spinning holder. The scattered light is collected by a set of lenses and guided into a CCD-camera equipped with a photography lens and a linear polarizer.*

angular spread of 1 degree between each two lines. This setup can effectively record patterns with angular spread of 30 degrees in total. This field of view is essential for measuring EBS of strongly-scattering samples such as porous-GaP ($k\ell < 10$).

For each sample, first a reference measurement is recorded on a weak sample such as Teflon ($k\ell \sim 100$). The narrow EBS-cone of the Teflon sample is effectively removed by fitting the measurement to a low order polynomial. This reference measurement is used to correct for the angular dependent transmittance of the beam-splitter. Then the sample is mounted on the spinning holder and the EBS from the sample is recorded. The normalized and axially averaged signal is then fitted by equation (A.1) with A, E_f, and $k\ell$ as 3 fitting variables. To demonstrate the precision of the measurements, the EBS recorded by this setup is compared with a rotating-arm setup, which is well-approved in the literature. This comparison is demonstrated in figure A.2. Note that the compact-CCD setup has higher resolution and less noise. It also has the potential of zooming at the center of the EBS cone for higher resolution.

For isotropic samples, EBS is axially symmetric. The recorded signal is then axially averaged for better speckle averaging. However, this setup has the potential of recording anisotropic EBS. In measuring an anisotropic sample, it should not be spined because the anisotropy will average out. Other methods of speckle averaging or broadband sources must be used for measuring an anisotropic EBS.

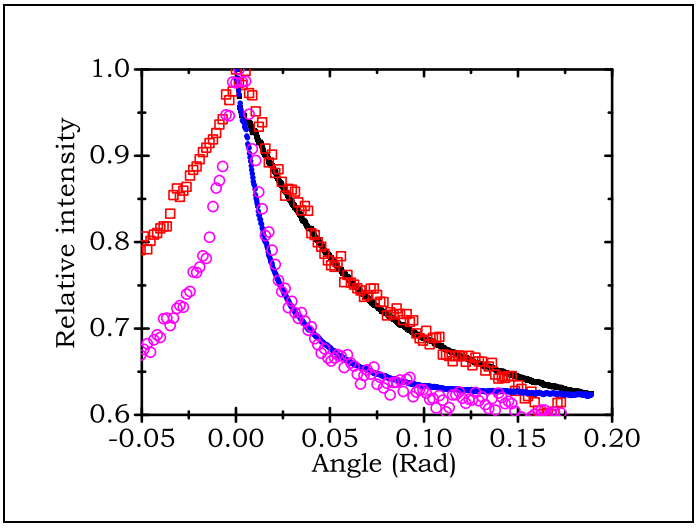

Figure A.2: *The enhanced backscattering recorded by the compact CCD setup is compared with the result obtained using the rotating-arm setup. Two different samples were analyzed. The open symbols show the measurements by rotating-arm setup and the closed symbols denote the result of CCD-setup measurements.*

APPENDIX B

Setup for total transmission measurement

The total transmission of light through an optically thick opaque slab is a well-accepted measure of the mean free path for isotropic scattering materials. The mean free path is generally dependent on the light frequency. Here I describe a setup I used to measure the mean free path of porous-GaP slabs in the visible and near infrared frequencies. This setup is sketched in figure B.1. It is possible to use this setup for measuring the total light transmitted through or reflected from the sample.

The light source is a fibre-laser(fianium) generating super-continuum in the 460-2500 nm spectral band. Several aluminum mirrors with proper attenuator filters in between guide the beam vertically into the entrance of a TiO_2 coated integrating sphere. The sample can be laid down at the entrance for transmission measurements or placed beneath the sphere for reflection measurements. At the exit aperture of the integrating sphere, a multi-mode optical fibre conveys the light signal to a spectrometer(Ocean Optics) connected to a PC. The spectrometer is most sensitive in the 500-1000 nm spectral band.

For each sample, first a reference spectrum is taken without the sample. This signal is just the scattered light from the TiO_2-coated bottom-cap of the integrating sphere. Then the sample is laid on top of the integrating sphere just in front of the entrance aperture, through which light enters the sphere. A second spectrum is recorded, which when divided by the reference spectrum, is a measure of total transmission. Then the bottom-cap of the sphere is removed and the sample is laid beneath the sphere. The scattered light from the sample is collected by the sphere and the third spectrum is recorded. Division of the third spectrum by the reference spectrum is a measure of total reflection. The reflection measurement is an additional option of the setup and is not used for determination of mean free path.

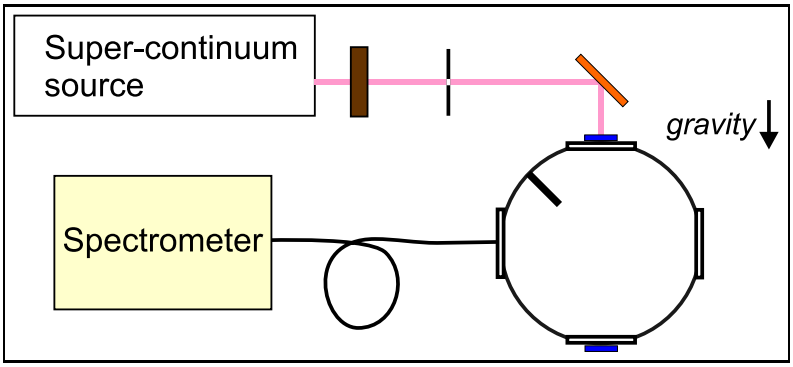

Figure B.1: *Schematic view of experimental setup for total transmission measurements. The opaque slab is illuminated with a parallel beam of 100 femtosecond pulses. The integrating sphere collects the scattered light at all angles on one side of the sample. The sample lies above the sphere for transmission measurements and beneath the sphere for reflection measurements. A multi-mode optical fibre connected to a CCD-coupled spectrometer reads the spectrum. Reflection from a thick TiO_2 layer is used as a reference.*

Index

Anderson localization, *see* Localization

Diffusion, 19
  anisotropic, 24, 44
  non-stationary, 29

Effusion
  point source, 26, 28
  transverse, 28, 45
Enhanced backscattering, 16

Gallium Phosphide, 35

Localization
  Anderson, 16
  transverse, 17
  weak, 16

Mean free path, 20, 38, 43
Method of images, 24

Nonlinear process, 30, 53

Phase matching, 30, 53
  quasi, 53
  random quasi, 53
Photo anodic etching, 36
Porosity, 37

Speckle, 21

Transmittance
  microscopy, 42
  plane wave, 25

The diffusion theory is very successful in explaining most of the effects that are observed in strongly scattering media. In the transition to the Anderson localization regime interference effects become so important that the diffusion theory will break down. Observation of Anderson localization of light is a holy grail for Optics researchers. Different experimental configurations have previously been proposed to check the limits of validity of the diffusion model for scattering media. Many of them have confirmed the agreement for weakly scattering materials and a few cases of deviation have been reported for the limit of strong scattering.

Nano-porous gallium phosphate sponges are among the most promising materials for observation of Anderson localization of light. Experimentally observing the breakdown of diffusion approximation for light propagation in GaP sponges can lead to the achievement of this aspiration.

Sanli Faez, June 2007, Amsterdam.